In situ determination of sulfur speciation and partitioning in aqueous fluid-silicate melt systems

A. Colin, C. Schmidt, G.S. S Pokrovski, M. Wilke, A.Y. y Borisova, M.J. Toplis

▶ To cite this version:

A. Colin, C. Schmidt, G.S. S Pokrovski, M. Wilke, A.Y. y Borisova, et al.. In situ determination of sulfur speciation and partitioning in aqueous fluid-silicate melt systems. Geochemical Perspectives Letters, 2020, 14, pp.31-35. 10.7185/geochemlet.2020 . hal-02905507

HAL Id: hal-02905507
https://hal.science/hal-02905507

Geochemical Perspectives
Letters

In situ determination of sulfur speciation and partitioning in aqueous fluid-silicate melt systems

A. Colin[1], C. Schmidt[2], G.S. Pokrovski[1*], M. Wilke[3], A.Y. Borisova[1,4], M.J. Toplis[5]

doi: 10.7185/geochemlet.2020

Abstract

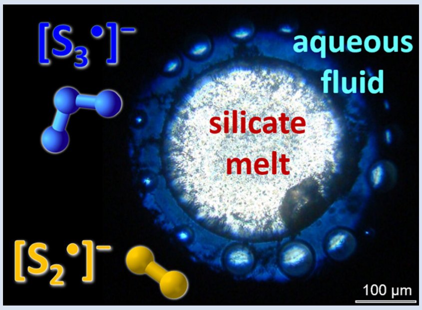

Current knowledge of sulfur behaviour in magmas is based exclusively on *ex situ* analyses. Here we report the first *in situ* measurement of sulfur speciation and partitioning between coexisting aqueous fluids and silicate melts. These data were acquired using Raman spectroscopy in a diamond anvil cell at 700 °C, 0.3–1.5 GPa, and oxygen fugacity in the vicinity of the sulfide-sulfate transition, conditions relevant to subduction zone magmatism. Results show that sulfate and sulfide are dominant in the studied systems, together with the $S_3^{\bullet -}$ and $S_2^{\bullet -}$ radical ions that are absent in quenched fluid and silicate glass products. The derived fluid/melt partition coefficients for sulfide and sulfate are consistent with those from available *ex situ* data for shallow crust conditions (<10 km), but indicate stronger partitioning of these sulfur species into the silicate melt phase with increasing depth. In contrast, both radical ions partition at least 10 times more than sulfate and sulfide into the fluid phase. Thus, by enhancing the transfer of sulfur and associated chalcophile metals from melt into fluid upon magma degassing, $S_3^{\bullet -}$ and $S_2^{\bullet -}$ may be important players in the formation of economic metal resources within the redox window of the sulfate-sulfide transition in subduction zone settings.

Received 11 September 2019 | Accepted 23 May 2020 | Published 10 July 2020

Introduction

The solubility, partitioning, and chemical speciation of sulfur in aqueous fluid-silicate melt systems are controlling factors in the processes of volatile and metal transfer and ore deposit formation in geodynamic settings associated with subduction zones. Our knowledge of these factors is currently based on *ex situ* analyses of fluids and melts brought to the Earth's surface or recovered in laboratory experiments upon cooling, such as volcanic sublimates and gases, fluid inclusions or silicate glasses. Yet, the complex and highly variable chemical and redox states of sulfur, spanning from S^{2-} (sulfide) to S^{6+} (sulfate), raise questions of how stable the different sulfur species are at temperatures (*T*) and pressures (*P*) relevant to magma generation and evolution, and how representative quenched natural and experimental samples are with regard to sulfur speciation and partitioning across the lithosphere. Indeed, along with coexisting sulfate and sulfide commonly observed in quenched samples, other previously disregarded species such as the tri- and disulfur radical ions, $S_3^{\bullet -}$ and $S_2^{\bullet -}$, become increasingly abundant in aqueous fluids above 200 °C but cannot be preserved upon cooling being unstable at ambient conditions (Pokrovski and Dubrovinsky, 2011; Schmidt and Seward, 2017). On the other hand, these radicals can bind to gold in hydrothermal fluids thereby enhancing the efficiency of gold supply to ore deposits (Pokrovski *et al.*, 2015; 2019). At shallow crust conditions (<0.3 GPa, <10 km depth), porphyry Cu-Mo-Re-Au and associated epithermal and skarn deposits, which are among the most significant resources of those metals on Earth, form in the vicinity of degassing magma bodies emplaced in the upper continental crust of arcs and back arc settings (Hedenquist and Lowenstern, 1994; Fontboté *et al.*, 2017). Although available natural silicate glass analyses, experimental data, and resulting models for sulfur in hydrous silicate melts provide a robust understanding of sulfur redox and partitioning at such conditions (*e.g.*, Moretti and Baker, 2008; Klimm and Botcharnikov, 2010; Wallace and Edmonds, 2011; Zajacz *et al.*, 2012; Zajacz, 2015; Binder *et al.*, 2018), much less is known about S redox and distribution in fluid-melt systems from lower crustal and upper mantle settings relevant to magma generation in subduction zones from which water, sulfur and metals for these deposits are sourced. At such depths (30–100 km, ~1–3 GPa), dehydration of the subducting slab generates aqueous fluids that can cause partial melting of the overlying mantle wedge (Hedenquist and Lowenstern, 1994; Richards, 2003). Such melts that become fluid saturated at some depth may carry and release significant amounts of

---

1. Group Fluids at Extreme Conditions (FLEX), Géosciences Environnement Toulouse (GET), Observatoire Midi-Pyrénées, Centre National de la Recherche Scientifique (CNRS), UMR 5563, Université de Toulouse, Institut de Recherche pour le Développement (IRD), 14 avenue Edouard Belin, 31400 Toulouse, France
2. Deutsches GeoForschungsZentrum (GFZ), Telegrafenberg, 14473 Potsdam, Germany
3. Universität Potsdam, Institut für Geowissenschaften, 14476 Potsdam, Germany
4. Geological Department, Lomonosov Moscow State University, Vorobievy Gory, 119899, Moscow, Russia
5. Institut de Recherche en Astrophysique et Planétologie (IRAP), Observatoire Midi-Pyrénées, Centre National de la Recherche Scientifique (CNRS), Université de Toulouse, 9 Avenue du Colonel Roche, 31400 Toulouse, France

* Corresponding author (email: gleb.pokrovski@get.omp.eu; glebounet@gmail.com)

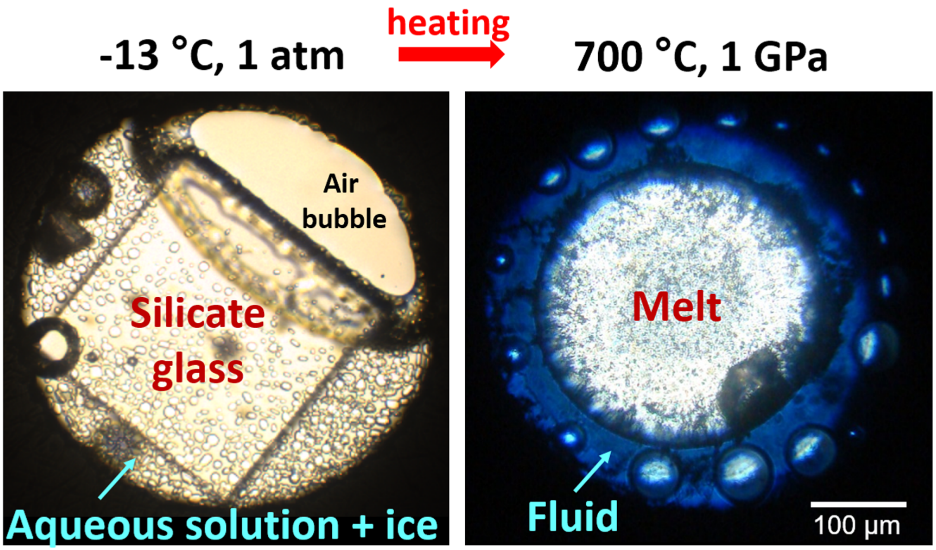

Figure 1 *In situ* approach applied in this study to determine sulfur speciation and partitioning in fluid-magma systems. A chip of silicate glass and aqueous thiosulfate solution are loaded in a diamond anvil cell (left), which is then heated to 700 °C and 0.3–1.5 GPa yielding a silicate melt and a blue aqueous fluid containing significant amounts of trisulfur radical ion (right). The coexisting phases are directly probed by micro-Raman spectroscopy and quantification based on Raman band intensities was performed using a method developed in this study (Supplementary Information).

sulfur-bound metals such as Au, Cu and Mo, whose fate strongly depends on the redox state and partitioning of sulfur itself between fluid and melt, during magma storage, evolution and transport across the subduction zone (*e.g.*, Richards, 2003; Audétat and Simon, 2012; Chelle-Michou *et al.*, 2017).

In an attempt to probe directly the sulfur chemical speciation and partitioning at the magmatic-hydrothermal transition, and to assess the impact of non-quenchable sulfur species such as $S_3^{\bullet-}$ and $S_2^{\bullet-}$ that cannot be studied using *ex situ* methods, we applied an *in situ* approach. Our method is based on Raman spectroscopy in a diamond anvil cell (DAC) and provides an unprecedented direct "window" into the identity, amount, and distribution of S species in fluid-magma systems (Supplementary Information). Here, we examined a set of four natural and synthetic silicate glasses, with SiO_2 contents from 50 to 75 mass % and alkalinity (Na + K)/Al (mol) from 0.6 to 3.0 (Tables S-1, S-2). Their composition has been chosen in this exploratory study to respond to three principal criteria: i) experimental feasibility, ii) relevance to the conditions of magma generation in subduction zones, and iii) possibility to cover a large range of silica content and alkalinity that are the major parameters controlling sulfur partitioning as seen by *ex situ* studies. The melts generated upon heating were equilibrated with sulfide/sulfate-bearing aqueous solutions at 700 °C and 0.3–1.5 GPa (Fig. 1).

Sulfur Speciation in the Coexisting Fluid and Melt Phases

Raman spectroscopy is the method of choice to study different sulfur species in fluids and melts owing to their characteristic and intense Raman scattering bands (Schmidt and Seward, 2017). The fluid phase at high *T-P* in all DAC experiments (Table S-2) shows Raman bands of water, dissolved silica species, and sulfate and sulfide (Fig. 2). In experiments with both sulfate and sulfide, the fluid displays a blue colour under white light illumination (Fig. 1), demonstrating the presence of the blue chromophore $S_3^{\bullet-}$ ion (Chivers and Elders, 2013). The Raman spectrum of the fluid phase indeed shows the characteristic

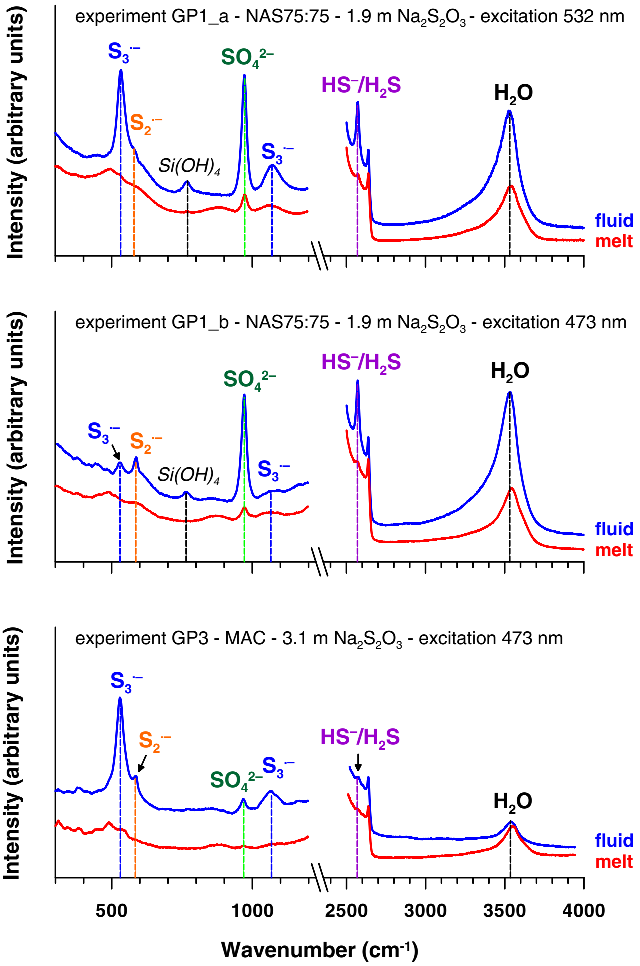

Figure 2 Raman spectra from representative experiments with indicated fluid and melt compositions, acquired at 700 °C and ~1 GPa with 473 and 532 nm excitation, and the major identified species.

vibrations of $S_3^{\bullet-}$ and $S_2^{\bullet-}$ ions, with signal intensity from $S_2^{\bullet-}$ increasing relative to that from $S_3^{\bullet-}$ in fluids in equilibrium with more alkaline melts (Fig. 2), in agreement with the reactions of $S_2^{\bullet-}$ and $S_3^{\bullet-}$ formation that are favoured at low and high proton activity, respectively:

$$13H_2S_{(aq)} + 3SO_4^{2-} = 8S_2^{\bullet-} + 2H^+ + 12H_2O_{(liq)} \qquad \text{Eq. 1}$$

$$19H_2S_{(aq)} + 5SO_4^{2-} + 2H^+ = 8S_3^{\bullet-} + 20H_2O_{(liq)} \qquad \text{Eq. 2}$$

The O–H stretching band of water in the spectra of silicate melts differs both in shape and position from that in spectra of the coexisting aqueous fluid. The melt spectra also show low intensity Si–O and Si–O–Si bands, similar to those in quenched glasses but distinct from those in the aqueous fluid (Figs. 2, S-3), thus supporting a negligible contribution of the fluid to the melt spectra. The species H_2S (and HS^-) and SO_4^{2-} are systematically detected in the silicate melt. The Raman signal from $S_3^{\bullet-}$ in the melt was quantified in two experiments (those with the highest S concentrations of >10 mass % S), whereas $S_3^{\bullet-}$ from S-poor experiments and $S_2^{\bullet-}$ in melts from all experiments were below detection (Figs. S-2, S-3, Table S-2).

In Situ Fluid/Melt Partition Coefficients of Sulfur Species

Our *in situ* data allow generation of the first direct set of fluid/melt partition coefficients, $D^{fl/mt}$(i), of each individual S species (where i = sulfate, sulfide, $S_3^{\bullet-}$, or $S_2^{\bullet-}$; Fig. 3, Table S-5). The $D^{fl/mt}$(sulfate) values are constant within measurement analytical uncertainties (1 standard deviation, s.d.) among the four studied melts, with an average of 17 ± 8 (1 s.d. of the mean) at 700 °C and 0.3–1.5 GPa, whereas the $D^{fl/mt}$(sulfide) values range from 6 ± 2 to 28 ± 8 (1 s.d.) from peraluminous to peralkaline melts, respectively (Fig. 3). Remarkably, the minimum $D^{fl/mt}$ values of both radical ions (50–450; Fig. 3) are at least a factor of 10 higher in favour of the fluid phase than those of sulfate and sulfide (see Supplementary Information for details of quantification). Thus, our *in situ* data reveal a much higher affinity of both radicals for the fluid phase compared to sulfate and sulfide, an important new finding that cannot be obtained using *ex situ* methods (see Supplementary Information for comparison with *ex situ* data).

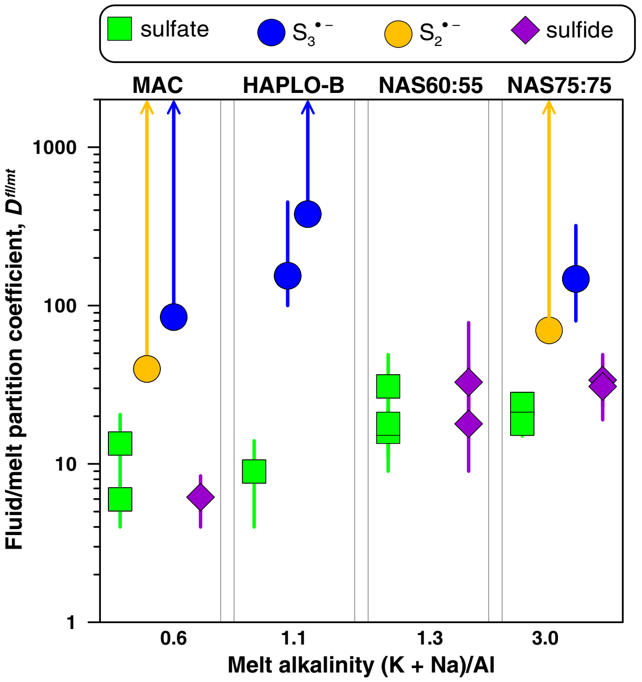

Figure 3 Partition coefficients (defined as the ratio of the species concentration in the fluid over its concentration in the silicate melt) at 700 °C and 0.3–1.5 GPa between fluid and melt for each sulfur species ($S_2^{\bullet-}$, $S_3^{\bullet-}$, sulfate and sulfide) for the indicated silicate melt compositions as a function of the initial alkalinity (Tables S-1, S-5; error bars 1 s.d.). Data points for the radical ions accompanied by arrowed vertical bars are minimal estimates corresponding to their detection limit in the melt.

Sulfur and Metal Transfer from Magmas to Ore Deposits in Subduction Zones

Our new findings provide insight into sulfur behaviour in subduction zone settings where fluid saturated melt generation, transfer and degassing can occur across a wide range of *T-P* and depth.

Firstly, our novel *in situ* data offer the advantage of direct estimation of sulfide and sulfate $D^{fl/mt}$ values for a given melt composition across a large f_{O2} range, because fluid/melt partitioning of an individual sulfur species is independent of f_{O2}. Our extrapolated values for melts of rhyolitic composition equilibrated with aqueous fluids at 0.3–1.5 GPa ($D^{fl/mt}$(sulfate) ~10 and $D^{fl/mt}$(sulfide) <10; Figs. 4, S-5) are a factor of 10 lower than those inferred from *ex situ* experiments performed at pressures of <0.5 GPa (see Supplementary Information) and analyses of natural glass inclusions trapped in volcanic rocks (*e.g.*, Wallace and Edmonds, 2011). Our results imply that felsic magmas, generated at depth and degassing through the lithosphere (10–45 km) both at highly reducing and highly oxidising conditions (*i.e.* outside the f_{O2} range within which the radical ions may be abundant), may retain more sulfur than was expected from *ex situ* analyses.

Secondly, our results demonstrate that both $S_2^{\bullet-}$ and $S_3^{\bullet-}$ ions are abundant in the S-rich fluid phase at the f_{O2} range of the sulfide-sulfate transition at temperatures of magma generation. First order estimates of the $S_3^{\bullet-}$ fraction in the experimental fluids of this study (700 °C, 1 GPa, 1–4 molal $Na_2S_2O_3$), amounting from 5 to 50 % of S_{tot}, are in good agreement with that predicted (Fig. S-8) using recent thermodynamic models based on *in situ* data at ≤500 °C (Pokrovski and Dubessy, 2015). The f_{O2} range favourable for both radicals matches that of the mantle wedge above the subducting slab where partial melting occurs. At these depths, back and forth changes in f_{O2} across the sulfate-sulfide transition window are common (Fig. 4). For instance, sulfate-dominated fluids, derived from subducted oceanic crust at >100 km depth, have the ability to oxidise the sulfide-bearing mantle wedge (*e.g.*, Evans, 2012; Walters *et al.*, 2020), by producing partial melts that rise up further to the mantle-crust boundary (70–40 km depth) and experience multiple phenomena (*e.g.*, Richards, 2003; Evans, 2012) as outlined in Figure 4. At higher crustal levels (5–15 km depth), mixing between sulfate-bearing felsic and FeS-bearing mafic melts may lead to S-rich magmas and fluids that are the major source of Au, Cu and Mo in porphyry deposits (Audétat and Simon, 2012). At shallower depths (<5 km), conduit flow modelling shows that degassing magmas rising to the surface in arc settings may evolve from reduced to oxidised, or oxidised to reduced, depending on their S content and initial f_{O2} (Burgisser and Scaillet, 2007). In summary, at different stages of their evolution, arc magmas are likely to cross the sulfide-sulfate transition

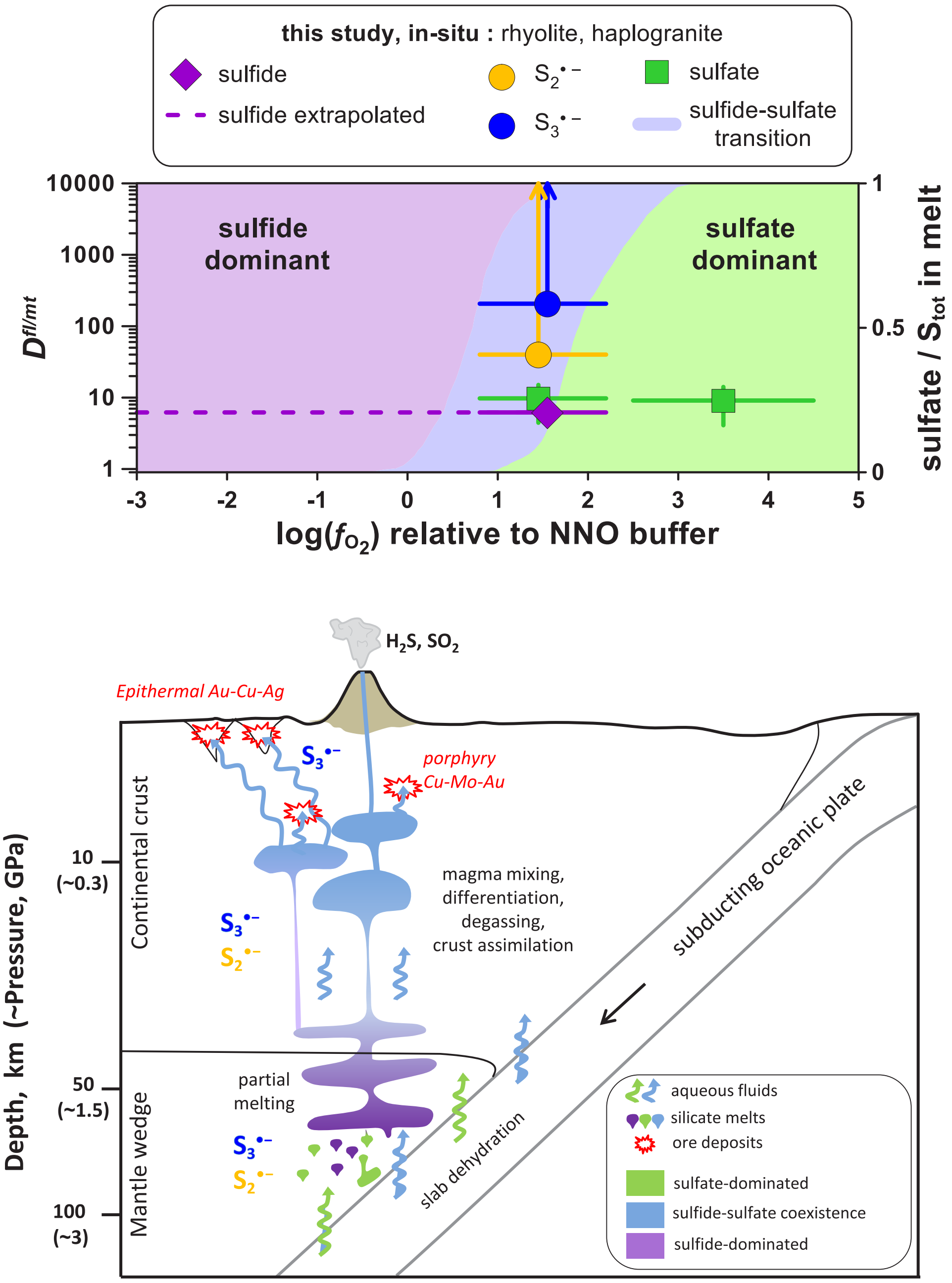

Figure 4 (Upper panel) *In situ* fluid/melt partition coefficients of sulfate, sulfide, $S_3^{\bullet -}$ and $S_2^{\bullet -}$, derived in this study for felsic melts (MAC, HAPLO-B) at 700 °C and 0.3–1.5 GPa as a function of f_{O2} (error bars 1 s.d.). Blue area outlines the sulfate-sulfide boundary in water saturated melt (Moretti and Baker, 2008); horizontal dashed line shows partition coefficients of sulfide extrapolated to the more reduced conditions of our *in situ* measurements. (Lower panel) Cartoon of a subduction zone setting (not to scale) schematically illustrating silicate melt and aqueous fluid generation and evolution, and the associated sulfur redox changes.

favouring formation of $S_2^{\bullet -}$ and $S_3^{\bullet -}$ (Fig. 4). Both radical ions partition at least 10 times more than sulfide and sulfate from felsic magmas into the volatile aqueous phase, thereby potentially enhancing sulfur degassing, depending on the initial fraction of sulfur in the form of radical ions in the melt (Fig. S-7) and total S content (S_{tot}) in the system (Fig. S-8), because $S_2^{\bullet -}$ and $S_3^{\bullet -}$ respective abundances are roughly a square and a cubic function of S_{tot}.

Thirdly, the strong enrichment of the fluid in radical ions compared to melt, coupled with the high affinity of $S_3^{\bullet -}$ and $S_2^{\bullet -}$ for gold (*e.g.*, Pokrovski *et al.*, 2019), and potentially for critical metals that have strong chemical bonds with sulfur (Pt, Pd, Mo, Re; *e.g.*, Laskar *et al.*, 2019), may be a key factor controlling trace metal transfer from the melt to the S-bearing fluid. Gold solubility in silicate melts displays a maximum at S^{6+}/S^{2-} ratios between 0.1 and 0.9 (Botcharnikov *et al.*, 2011; Zajacz *et al.*, 2012), implying enhanced gold extraction from the mantle by magmas generated by partial melting of the mantle wedge at such redox conditions. Upon ascent and degassing of such Au pre-enriched magma, this gold is remobilised and concentrated by the released $S_3^{\bullet -}$-bearing fluids. According to Eqs. 1 and 2, the concentrations of the di- and trisulfur ions are maximised both in melt and fluid at sulfide:sulfate ratios of 13:3 and 19:5, respectively (corresponding to ~80 % of S_{tot} as sulfide). Such sulfide-dominated, yet moderately oxidised, systems are common in arc magma settings that host major porphyry-epithermal

Cu-Mo-Au deposits (Fontboté *et al.*, 2017). According to the most conservative estimates of the $D^{fl/mt}(S_3^{\bullet-})$ values in this study (~100), a melt containing only 10 µg/g S in the form of $S_3^{\bullet-}$ would produce 1000 µg/g S as $S_3^{\bullet-}$ in the fluid at equilibrium. Such concentrations of trisulfur ion are largely sufficient to bind to trace metals, extract them from the magma, transport them in the fluid phase to ore deposition sites, and control the deposition due to $S_3^{\bullet-}$ destabilisation upon fluid cooling, boiling or interaction with rocks. Our study thus reveals that sulfur radical ions may be key players in the formation of economic metal resources within the redox window of the sulfate-sulfide transition across subduction zone settings.

Acknowledgements

This work was funded by the French National Research Agency (grants RadicalS, ANR-16-CE31-0017), the Institut Carnot ISIFoR (grant OrPet), and the French and German embassies (grant PHC Procope SulFluMag). We thank T. Aigouy, P. Besson, J. Buhk, A. Castillo, P. Gisquet, S. Gouy, M. Kokh, J.-F. Ména, F. de Parseval, P. de Parseval, and S. Moyano for their help with sample preparation and analyses, A.-M. Cousin for her help with figure layout, W.A. Bassett for advice on DAC techniques, G. Harlow, J. Newman and B. Ledé for providing lazurite samples, and K. Kiseeva for discussions. Constructive comments of Editor H. Marschall and reviewers Z. Zajacz and C. LaFlamme greatly improved this article. We are grateful to A. Williams and M.-A. Hulshoff for editorial management.

Editor: Horst R. Marschall

Additional Information

Supplementary Information accompanies this letter at http://www.geochemicalperspectivesletters.org/article2020.

Cite this letter as: Colin, A., Schmidt, C., Pokrovski, G.S., Wilke, M., Borisova, A.Y., Toplis, M.J. (2020) *In situ* determination of sulfur speciation and partitioning in aqueous fluid-silicate melt systems. *Geochem. Persp. Let.* 14, 31–35.

References

Audétat, A., Simon, A.C. (2012) Magmatic controls on porphyry copper genesis. *Society of Economic Geologists Special Publication* 16, 553–572.

Binder, B., Wenzel, T., Keppler, H. (2018) The partitioning of sulfur between multicomponent aqueous fluids and felsic melts. *Contribution to Mineralogy and Petrology* 173, 18.

Botcharnikov, R., Linnen, R.L., Wilke, M., Holtz, F., Jugo, P.J., Berndt, J. (2011) High gold concentrations in sulphide-bearing magma under oxidizing conditions. *Nature Geoscience* 4, 112–115.

Burgisser, A., Scaillet, B. (2007) Redox evolution of a degassing magma rising to the surface. *Nature* 445, 194–197.

Chelle-Michou, C., Rottier, B., Caricchi, L., Simpson, G. (2017) Tempo of magma degassing and the genesis of porphyry copper deposits. *Scientific Reports* 7, 40566.

Chivers, T., Elder, P.J.W. (2013) Ubiquitous trisulfur radical ion: fundamentals and applications in materials science, electrochemistry, analytical chemistry and geochemistry. *Chemical Society Reviews* 42, 5996–6005.

Evans, K.A. (2012) The redox budget of subduction zones. *Earth Science Reviews* 113, 11–32.

Fontboté, L., Kouzmanov, K., Chiaradia, M., Pokrovski, G.S. (2017) Sulfide minerals in hydrothermal deposits. *Elements* 13, 97–103.

Hedenquist, J.W., Lowenstern, J.B. (1994) The role of magmas in the formation of hydrothermal ore deposits. *Nature* 370, 519–527.

Klimm, K., Botcharnikov, R.E. (2010) The determination of sulfate and sulfide species in hydrous silicate glasses using Raman spectroscopy. *American Mineralogist* 95, 1574–1579.

Laskar, C., Pokrovski, G.S., Kokh, M.A., Hazemann, J.-L., Bazarkina, E.F., Desmaele, E. (2019) The impact of sulfur on the transfer of platinoids by geological fluids. *Abstracts of the Goldschmidt 2019 Conference, Barcelona, Spain*, 1831 ⟨hal-02343794⟩.

Moretti, R., Baker, D.R. (2008) Modeling the interplay of fO_2 and fS_2 along the FeS-silicate melt equilibrium. *Chemical Geology* 256, 286–298.

Pokrovski, G.S., Dubrovinsky, L.S. (2011) The S_3^- ion is stable in geological fluids at elevated temperatures and pressures. *Science* 331, 1052–1054.

Pokrovski, G.S., Dubessy, J. (2015) Stability and abundance of the trisulfur radical ion in hydrothermal fluids. *Earth and Planetary Science Letters* 411, 298–309.

Pokrovski, G.S., Kokh, M.A., Guillaume, D., Borisova, A.Y., Gisquet, P., Hazemann, J.-L., Lahera, E., Del Net, W., Proux, O., Testemale, D., Haigis, V., Jonchière, R., Seitsonen, A.P., Ferlat, G., Vuilleumier, R., Saitta, A.M., Boiron, M.-C., Dubessy, J. (2015) Sulfur radical species form gold deposits on Earth. *Proceeding of the National Academy of Sciences of the U.S.A.* 112, 13484–13489.

Pokrovski, G.S., Kokh, M.A., Proux, O., Hazemann, J.-L., Bazarkina, E.F., Testemale, D., Escoda, C., Boiron, M.-C., Blanchard, M., Ajgouy, T., Gouy, S., de Parseval, P., Thibaut, M. (2019) The nature and partitioning of invisible gold in the pyrite-fluid system. *Ore Geology Reviews* 109, 545–563.

Richards, J.P. (2003) Tectono-magmatic precursors for porphyry Cu-(Mo-Au) deposit formation. *Economic Geology* 98, 1515–1533.

Schmidt, C., Seward, T.M. (2017) Raman spectroscopic quantification of sulfur species in aqueous fluids: Ratios of relative molar scattering factors of Raman bands of H_2S, HS^-, SO_2, $HSO_4{}^-$, $SO_4{}^{2-}$, $S_2O_3{}^{2-}$, $S_3{}^-$ and H_2O at ambient conditions and information on changes with pressure and temperature. *Chemical Geology* 467, 64–75.

Wallace, P.J., Edmonds, M. (2011) The sulfur budget in magmas: evidence from melt inclusions, submarine glasses and volcanic emissions. *Reviews in Mineralogy and Geochemistry* 73, 215–246.

Walters, J.B., Cruz-Uribe, A.M., Marschall, H.R. (2020) Sulfur loss from subducted altered crust and implications for mantle oxidation. *Geochemical Perspectives Letters* 13, 36–41.

Zajacz, Z. (2015) The effect of melt composition on the partitioning of oxidized sulfur between silicate melts and magmatic volatiles. *Geochimica et Cosmochimica Acta* 158, 223–244.

Zajacz, Z., Candela, P.A., Piccoli, P.M., Wälle, M., Sanchez-Valle, C. (2012) Gold and copper in volatile saturated mafic to intermediate magmas: Solubilities, partitioning, and implications for ore deposit formation. *Geochimica et Cosmochimica Acta* 91, 140–159.

Geochemical Perspectives Letters

In situ determination of sulfur speciation and partitioning in aqueous fluid - silicate melt systems

A. Colin, C. Schmidt, G.S. Pokrovski, M. Wilke, A.Y. Borisova, M.J. Toplis

Supplementary Information

The Supplementary Information includes:

- 1. Materials and Methods
- 2. Supplementary Text: Additional Notes
- Tables S-1 to S-8
- Figures S-1 to S-8
- Supplementary Information References

1. Materials and Methods

1.1. Summary

We have developed a method to quantify the partitioning of different sulfur species between coexisting aqueous fluid and silicate melt using Raman spectra of these species acquired from each coexisting phase *in situ* at high temperatures and pressures in a diamond-anvil cell (DAC). The investigated silicate glasses (Section 1.2; Table S-1) span wide ranges of silica content ($50 < SiO_2 < 75$ mass %) and alkalinity ($0.6 < (Na + K) / Al < 3.0$), and include a natural rhyolite (MAC, an obsidian from the Macusani volcano; Borisova *et al.*, 2010), two synthetic glasses in the Na_2O-Al_2O_3-SiO_2 system (NAS75:75 and NAS60:55, equivalent to a peralkaline rhyolite and a phonolite, respectively; Toplis *et al.*, 1997) and a synthetic haplogranite glass doped with boron (HAPLO-B, representative of granitic rocks associated with Sn(-W) mineralisation; Pichavant, 1987; Heinrich, 1990). Aqueous sodium thiosulfate ($Na_2S_2O_3$), sulfuric acid (H_2SO_4), and sodium sulfate (Na_2SO_4) solutions of 0.2 to 3.5 molal were used as the source of sulfur. The use of thiosulfate constrains the redox potential (fO_2) in the system and the acidity (pH) in the fluid phase via equilibria among the abundant sulfide and sulfate species (HS^-/H_2S and HSO_4^-/SO_4^{2-}), which are produced by $S_2O_3^{2-}$ breakdown on heating (Jacquemet *et al.*, 2014). A chip of silicate glass of controlled size and thickness, a pressure sensor (zircon), and an S-bearing aqueous solution were loaded in an externally heated Bassett-type DAC equipped with ultra-low fluorescence diamond anvils and an iridium gasket (Bassett *et al.*, 1993; Schmidt and Chou, 2012; Schmidt *et al.*, 2013). The loaded S and salt concentrations were accurately determined by measuring the vapour-saturated liquidus temperature of the aqueous solution frozen in the cell (Section 1.3). The cell was heated until melting of the silicate glass at T of 700 °C and P of ~0.3–1.5 GPa (Fig. 1). Raman spectra were acquired through the diamond window from the coexisting fluid and melt phases using 473 and 532 nm excitation lasers to better quantify the radical species whose Raman signal is strongly wavelength-dependent due to a resonance phenomenon (Ledé *et al.*, 2007; Pokrovski and Dubessy, 2015). Raman intensities were corrected as described by Schmidt and Seward (2017) to allow quantification based on spectra recorded at different conditions. The partition coefficient $D^{fl/mt}$(i) of each sulfur species (i) between the coexisting fluid and silicate melt was determined from the ratio of relative integrated intensities of the most intense Raman band of each species in the fluid and melt phases, corrected for the phase densities and absorbance of the Raman signal by the chromophore S radical ions, and adopting the same Raman scattering cross sections for a given species in both phases (Sections 1.4-1.6). Furthermore, in selected DAC experiments, the silicate melt, quenched at the end of the run, was recovered and analysed with electron probe micro analyzer (EPMA) for major element and sulfur content. In addition, independent experiments between the same silicate melts and S-bearing solutions were performed at 0.3 GPa and 700 °C using a traditional *ex situ* batch-reactor method employing quenching. *Ex situ* total sulfur partition coefficients were derived from EPMA analyses of the quenched glasses and mass balance calculations for S content of the fluid phase (Section 1.7; Tables S-6 and S-7). Chemical equilibrium calculations using recently derived and updated thermodynamic properties of aqueous sulfur species (Pokrovski and Dubessy, 2015; Pokrovski *et al.*, 2019) have been conducted to predict the abundance of the different sulfur species in the aqueous thiosulfate solutions used in this study and compare these estimations with the Raman-derived values (Section 1.8).

1.2. Silicate glass choice, synthesis and composition

The silicate glass samples chosen for this exploratory study respond to the three major criteria: i) technical and experimental feasibility, ii) pertinence and representativeness to the geodynamic settings of magma generation in subduction zones, and iii) possibility to cover a large range of magma compositions, in particular the silica content and alkalinity, which are the major parameters controlling sulfur partitioning patterns as has been shown in numerous *ex situ* studies. To avoid intrinsic technical difficulties related to the use of *in situ* DAC methods at high temperatures, we used relatively simple felsic and alkaline silicate glass compositions having relatively low melting temperatures (700 °C), to be able to accurately produce and keep the melt phase in the experiments. These compositions are, nevertheless, typical of those produced by partial melting of subducted sediments of pelitic compositions and basalts in the presence of water as found in previous work (Section 2.2). To allow accurate method development, which is aimed to set up novel approaches for *in situ* Raman spectroscopy measurements in fluid-melt systems, we intentionally use relatively simple melt compositions, which were Fe- and Ca-free to avoid eventual formation of FeS and $CaSO_4$ that might complicate the straightforward interpretation of our exploratory measurements. Nevertheless, our compositions cover a wide range of SiO_2 contents and alkalinity allowing us to establish first *in situ* trends in partition coefficients and to accurately compare them with available previous work. The detailed characteristics of each chosen glass sample are given below.

Four silicate glasses were used for sulfur partitioning experiments (Table S-1): two synthetic glasses of Na_2O-Al_2O_3-SiO_2 composition, analogous to a peralkaline rhyolite (NAS75:75) and a phonolite (NAS60:55), a natural obsidian from Macusani volcano, SE Peru (MAC) and a synthetic haplogranite glass doped in boron (HAPLO-B). NAS75:75 and NAS60:55 glasses were synthesised from reagent-grade oxides mixed in an agate mortar, melted in a platinum crucible for 1 h above the liquidus, quenched, crushed, and then reheated at 1700 °C for 2 h while stirring to eliminate residual air bubbles and, finally, quenched (Toplis *et al.*, 1997). MAC glass is a natural aphyric obsidian of rhyolitic peraluminous composition, representative of anatectic melts derived from metasedimentary crustal protoliths and analogous to highly differentiated Li-rich pegmatites, which are the ultimate products of fractionation of S-type granitic magmas enriched in B, P, and F (Borisova *et al.*, 2010). HAPLO-B is a peraluminous haplogranite glass doped in boron whose composition has the lowest liquidus temperature in the quartz-albite-orthoclase system at H_2O-saturated conditions (640 °C, 0.1 GPa, 4.5 mass % B_2O_3; Pichavant, 1987). Its composition is typical of granitic rocks enriched in B that host hydrothermal Sn(-W) ore deposits (Heinrich, 1990). The glass was synthesised by grounding appropriate amounts of reagent grade SiO_2, Al_2O_3, K_2CO_3, Na_2CO_3 and B_2O_3 in an agate mortar and melting the mixture twice during 2 h at 1400 °C. Part of the product ground into powder was dissolved in HF and analysed by Inductively Coupled Plasma - Atomic Emission Spectroscopy (ICP-AES) for P, Na, B and K; then the composition of the product was adjusted by addition of oxides to compensate for some loss of the volatile elements, and the mixture was melted again for 2 h at 1400 °C. A chip of the final glass was analysed for SiO_2, Al_2O_3, Na_2O and K_2O by electron microprobe (EPMA), and B_2O_3 content was estimated as the difference between the totals and 100 mass % (Table S-1).

1.3. DAC setup and *in situ* Raman spectroscopy experiments

1.3.1. Experimental setup

An externally heated Bassett-type diamond anvil cell (DAC; Bassett *et al.*, 1993; Schmidt, 2009; Fig. S-1), equipped with ultra-low fluorescence grade diamond anvils with a culet diameter of 0.9 mm, was used in this study. The diamonds are inserted into the heaters, which consist of NiCr wires wound around tungsten carbide seats and insulated with alumina cement. The temperature was continuously measured by K-type thermocouples attached to the anvils and controlled using Eurotherm 2408 temperature controllers. The thermocouples were calibrated by measuring the temperature of the α-β transition of quartz at 574 °C, 0.1 MPa (Schmidt and Chou, 2012). The Raman spectra were recorded with a HORIBA Jobin Yvon LabRAM HR800 Vis Raman spectrometer (grating 1800 lines/mm, focal length 800 mm, confocal pinhole 1000 µm, slit aperture 100 µm), equipped with a Synapse back-illuminated CCD detector (2048 × 512 pixels) and an Olympus BXFM microscope with a motorised XYZ sample stage. The unpolarised spectra were acquired in backscattering geometry using an Olympus SLMPlan N 20× objective with a working distance of 25 mm. A COBOLT Blues™ DPSS laser (wavelength 473 nm, power stability <2 %), or a Laser Quantum Torus 532 DPSS laser (wavelength 532 nm, power stability <1 %), were used for Raman scattering excitation. The 473 nm and 532 nm laser power measured at the microscope objective before each analytical session was ~10 mW and ~25 mW, respectively.

1.3.2. Experimental protocol

A chip of silicate glass was loaded into an iridium gasket hole (internal diameter 400 µm, thickness 125 µm), together with a small chip of synthetic Hf-doped zircon for pressure determination ($Zr_{0.99}Hf_{0.01}SiO_4$; Schmidt *et al.*, 2013), and a droplet of sulfur-bearing aqueous solution. Special attention was paid to load a piece of glass with a thickness close to that of the iridium gasket, to allow the resulting melt to fill the full cell thickness without the aqueous fluid phase on top. For this purpose, doubly polished, ~100 µm thick glass sections were cleaned with acetone and ethanol to remove any residual organics, and cut in square shapes either using a UV femtosecond pulsed laser ablation system (experiments GP1–GP8) or a diamond cutter (GP9–GP17). After loading, the cell was loosely closed to allow an air bubble to grow to a volume of 15-50 % of that of the solution. Taking the solute concentrations into account, the resulting fluid density is 0.9–1.2 g/cm^3 in the range 0.3–1.5 GPa at 700 °C, as estimated using the PVTX properties of the fluid phase (see below). The cell was then sealed and the salt content of the loaded solution, which usually significantly deviated from that of the original solution, was determined by cryometry. This determination is required because it is difficult to avoid significant solution evaporation during the cell loading and bubble growth, as the volumes are extremely small. For cryometry measurements, the fluid was frozen at −40 °C using liquid nitrogen. Then the cell was allowed to slowly warm up and the temperature of disappearance of the last crystals in the solution (measured to ±0.2 °C) was used to determine the salt concentration using the known freezing temperature versus molality (m) dependences for aqueous sodium pentahydrate thiosulfate (Picon, 1924) and sodium sulfate (Linke and Seidell, 1965) solutions. The uncertainty of the concentration determination for our solute compositions is less than ± 0.1 m.

The DAC was flushed with an Ar + 1% H_2 gas mixture to prevent oxidation of the diamonds and the heating resistances at high temperature. Raman spectra were acquired from the coexisting fluid and melt phases in the 200–1200 cm^{-1} and 2500–4000 cm^{-1} ranges, which contain the studied known vibrational modes of sulfur species and water while avoiding the intense C-C band from the diamond anvils. The laser focus was consistently set to 20 µm below the surface of the top anvil to maximise the Raman signal (Everall, 2000; Schmidt and Chou, 2012). During a typical experiment, a Raman spectrum of the aqueous solution was recorded at room temperature; then the temperature was first slowly increased to the homogenisation point identified by the disappearance of the air bubble clearly visible under the microscope, and then the temperature was set at 700 °C (Table S-2). During the heating, the $S_3^{\bullet-}$ ion in the fluid was clearly identified by its characteristic intense blue color. Once the temperature reached 700 °C, a Raman spectrum of zircon was acquired to determine the pressure based on the P-dependent shift of the Raman band from antisymmetric SiO_4 stretching vibration at ~1000 cm^{-1} (Schmidt *et al.*, 2013). In four experiments where zircon was absent (GP1_a, GP1_b, GP6, GP7), P was estimated based on the homogenisation temperature during heating and using the PVTX properties of the NaCl-H_2O system (Driesner, 2007), and assuming that the density of a thiosulfate solution is similar to that of a NaCl solution of the same mass concentration; this approximation induces an error of less than 10 % of the total P value at our salt concentrations (*e.g.*, Pokrovski *et al.*, 2009). Then spectra of the fluid and melt were recorded (typically 5 accumulations of 20 s each) over a 0.5–2.0 h interval to check for the attainment of equilibrium. Care was taken to avoid nucleation of fluid bubbles while recording the melt spectrum by decreasing the laser power by a factor of

10 compared to that used for the fluid phase spectrum (and accordingly increasing acquisition time). It was found that Raman integrated intensity peak ratios recorded successively for a given species in the coexisting fluid and melt were constant within errors (see below) over the run time, suggesting a fast equilibrium attainment (few minutes), favoured by strong fluid-melt convection, systematically observed in the cell and likely induced by small T gradients (<1 °C). The convection was visible via the microscope camera during the experiment and consisted in bubbles of fluids continuously nucleating in the melt and then growing and coalescing with the rest of the fluid in a timescale of 10s sec. The fluid/melt Raman peak ratios for a given S species measured within a short time interval (<10 min) were insensitive to the eventual decrease of the $S_3^{\bullet-}$ and H_2S Raman peak intensities in the fluid phase observed in some experiments (GP15, GP17) over much longer time intervals (1–2 h), likely due to a slow reaction of reduced sulfur species with the iridium gasket. Thus, even though quantification of the species absolute concentrations in the two phases is difficult in these experiments, the peak ratios fairly accurately reflect the distribution of the sulfur species between the two phases. Upon completion of measurements at 700 °C, the temperature was dropped in a few seconds to ~400 °C to quench the melt and limit water exsolution, followed by slower cooling to vapor-liquid immiscibility temperature, which was always reproducible within <10 °C with the value obtained on heating. The quenched glass phase was recovered in some experiments (where possible) for *ex situ* analyses of total S content (Section 1.7).

1.3.3. *Raman bands of the detected sulfur species*

Raman spectra of the fluid phase in most experiments show a prominent band of the OH vibrations of water (2800–3800 cm^{-1}), Si-O-Si and Si-OH vibrations of dissolved silica species, such as $Si(OH)_4$ and its dimer (400–800 cm^{-1}) (Steele-MacInnis and Schmidt, 2014), and the symmetric stretching vibration of sulfate (960–980 cm^{-1}, corresponding to the SO_4^{2-} ion and its ion pairs with Na^+; Schmidt and Seward, 2017), and sulfide (HS^-, H_2S, 2570–2590 cm^{-1}; Schmidt and Seward, 2017) (Table S-2). In runs with coexisting aqueous sulfate and sulfide, the fluid phase displays a bright to dark blue color above 400 °C (Fig. 1), demonstrating the presence of the blue chromophore $S_3^{\bullet-}$ ion (Pokrovski and Dubrovinsky, 2011; Chivers and Elder, 2013). The Raman spectrum of the fluid shows a clear signature of $S_3^{\bullet-}$ with a resonant symmetric stretching vibration band at 535±5 cm^{-1} and its overtone at 1070±10 cm^{-1} (Fig. 2). The $S_3^{\bullet-}$ band has a shoulder at 585±5 cm^{-1} that belongs to the stretching vibration of the disulfur radical ion $S_2^{\bullet-}$ whose resonance signal is favoured with 473 nm excitation (*e.g.*, Pokrovski and Dubessy, 2015). The spectra of silicate melts have a pronounced water band (2800–3800 cm^{-1}), different in shape and position from that in aqueous fluid, and two broad low-intensity features in the range 500–600 cm^{-1} arising from the silicate network, similar to those reported in quenched glasses (Le Losq *et al.*, 2014) but distinct from those in the aqueous fluid (Fig. 2, Fig. S-3), confirming negligible contribution of the fluid in the melt spectra. The species H_2S (and HS^-) and SO_4^{2-} are present in melt, with similar Raman band positions but lower intensities compared to those in the coexisting fluid (Fig. 2 and Table S-2). Note that the fully deprotonated sulfide ion S^{2-} suggested to form in silicate melts by some *ex situ* studies cannot directly be probed by Raman spectroscopy; however, it is virtually non-existent in aqueous solution (Pokrovski and Dubessy, 2015) and thus is unlikely to be important in the H_2O-saturated silicate melts of the present study. The $S_3^{\bullet-}$ Raman signal is clearly detected in the melt in two experiments with the highest S concentrations (>10 mass % S; runs GP1, GP16 in Fig. S-3) using the 532 nm laser, enhancing the $S_3^{\bullet-}$ resonance signal. The signals of $S_3^{\bullet-}$ in melts from experiments with lower S concentration and of $S_2^{\bullet-}$ in melts from most experiments were below detection (Table S-2).

1.4. Derivation of $D^{fl/mt}$ values of individual sulfur species from *in situ* measurements

1.4.1. *Definition of Raman spectra corrections and partition coefficient* $D^{fl/mt}$

Raman spectra were corrected following Schmidt and Seward (2017):

$$I_{corr,\omega} = \frac{I_{ICS,\omega}}{t \times P_{laser} \times F_{\omega} \times (B+1)} \qquad \text{(Eq. S-1)}$$

where $I_{ICS,\omega}$ is the intensity corrected for the response function of the spectrometer (as determined from the manufacturer) at the given Raman shift ω (i.e. the wavenumber difference of the scattered radiation relative to the excitation light ω_{laser}, in cm^{-1}), t is the acquisition time (s), P_{laser} is the laser power at the objective (mW), F_{ω} is the frequency-dependent scattering factor $F_{\omega} = (\omega_{laser} - \omega)^3 \times \omega^{-1}$, and $(B + 1)$ is the temperature dependence function of the Stokes Raman scattering intensity $(B + 1) = 1/(1 - e^{-h \times c \times w/(k_B \times T)})$, where h is the Planck constant, c is the speed of light, k_B is the Boltzmann constant, and T is the temperature in Kelvin. These corrections are important for comparisons of spectra recorded at different temperatures and with different lasers and acquisition times, and furthermore facilitate the comparison with literature data acquired at different conditions (Schmidt and Seward, 2017).

The corrected spectra were used to calculate the partition coefficient $D^{fl/mt}(\mathrm{i})$ of the sulfur species i between the fluid and the silicate melt, i.e. the ratio of the species concentration in the fluid over its concentration in the silicate melt:

$$D^{fl/mt}(\mathrm{i}) = \frac{C_{i,fluid}}{C_{i,melt}} \cong \frac{A_{i,fluid} \times d_{melt} \times \gamma_i}{A_{i,melt} \times d_{fluid}} \qquad \text{(Eq. S-2)}$$

where C_i is the species mass concentration in each phase, A_i is the integrated intensity of the most intense Raman band of i-th species in fluid or melt, d is the fluid or melt density, and γ_i is a factor correcting for the absorbance of the chromophore species $S_3^{\bullet-}$ (where present) at the given Raman shift ω with λ_0 excitation.

No correction was applied for the difference of refractive indexes at the silicate melt-diamond and fluid-diamond interfaces, since solute-rich aqueous fluids and water-saturated silicate melts have relatively close refractive indexes. Details on the determination of the integrated Raman intensities, phase densities, and absorbance are given below.

1.4.2. Raman peak fitting

Spectra were processed using the Fityk 1.2.0 software (Wojdyr, 2010) (Fig. S-2). A cubic spline was manually defined to fit the baseline far from the peak areas and was subtracted from the spectrum. Then Raman bands were fitted using pseudo-Voigt models (that are a convolution of a Cauchy-Lorentz distribution and a Gaussian distribution). The peak shape (ratio Gaussian/Lorentzian) was arbitrary fixed at 0.5, which is a common choice for Raman peaks and has a very minor impact on the fitted peak areas (*e.g.*, Dargent *et al.*, 2013). Small bands are difficult to extract in regions where the baseline is not linear or multiple bands overlap. For instance, the main Raman bands of sulfur radical ions occur in the same wavenumber region as those of Si-O-Si groups. In cases where the Raman band of interest was close to or below detection limit, in particular in the melt, the main overlapping peaks were fitted first and subtracted from the overall signal; then a range of acceptable values for the area of the small peak of interest was defined by manually adjusting the height of a pseudo-Voigt peak with parameters (Full Width at Half Maximum, FWHM, and pseudo-Voigt peak center) identical to those determined in the fluid in which the sulfur species peaks are usually far more pronounced. For example, in experiment GP3, S radicals were below detection limit in the melt (Fig. S-3), which was defined as the integrated intensity of the largest $S_3^{\bullet-}$ and $S_2^{\bullet-}$ bands at 532 cm^{-1} and 585 cm^{-1}, respectively, that would reasonably match the spectral background dominated by the Si-O-Si signal. When the Raman peak was not easily extractable from the baseline, like in case of sulfide whose Raman peak is situated on the shoulder of the diamond overtone (~ 2500 cm^{-1}), the curvature of the baseline was manually varied within reasonable positions based on baselines in sulfide-free experiments to define a maximum area for H_2S/HS^- bands; FWHM and peak centers were also taken identical to those in the phase (usually the fluid) where the peaks are well defined. An example of the peak fitting procedure is shown in Figure S-2, and examples of baseline-corrected Raman spectra in the low-frequency region (<1200 cm^{-1}) of the fluid and melt phases are given in Figure S-3.

Identifying the dissolved silicate Raman signals is necessary for accurate background corrections of the spectra of sulfur species whose bands overlap. Dissolved silicate are systematically identified in the 400–700 cm^{-1} region by broad Raman bands that belong to bending vibrations of the bridging oxygen Si-O-Si groups. The main bands are centered at ~450, 550 and 600 cm^{-1}, in agreement with the data of Steele-MacInnis and Schmidt (2014) on H_2O-Na_2O-SiO_2 fluids (Fig. S-3, see experiment GP7, where Si-O-Si bands are unambiguously identified in the transparent, $S_3^{\bullet-}$-free fluid). The presence of vibration bands of sulfur species in the 700–1000 cm^{-1} region, and the low Raman intensities in concentrated colored solutions containing large amounts of $S_3^{\bullet-}$ ion do not allow unambiguously identifying silicate species in such fluids. In contrast, in the Raman spectra of more S-dilute fluids equilibrated with felsic melts (NAS75:75, MAC, HAPLO-B), a peak was clearly visible at 770 cm^{-1} (*e.g.*, experiment GP1, Fig. S-3) and was assigned to the Si-OH symmetric stretching vibration of $Si(OH)_4$ monomers (Q_0). In fluids equilibrated with the melt of intermediate composition (NAS60:55), the fluid spectra exhibit a broad band at 770–870 cm^{-1} (*e.g.*, experiment GP7, Fig. S-3) that might be due to a contribution of Q_1–Q_3 silicate species. According to Steele-MacInnis and Schmidt (2014), the predominance of Q_0 monomers is typical for fluids with relatively low SiO_2 concentrations (< 7 mol %) whereas the dominant presence of Q_1–Q_3 species indicates polymerised and thus more silica-concentrated fluids.

1.4.3. Density correction

In the melt phase, the molar volume of the silicate melt at the run conditions (700 °C, 0.3–1.5 GPa) was calculated as the weighted average of the molar volumes of an equivalent anhydrous melt and of water dissolved in high pressure silicate melts. For anhydrous melts, the Glass Density Calc v3.2 Excel spreadsheet (Lange and Carmichael, 1990; Iacovino, 2017) was used, considering the initial composition of the glasses. Boron was not considered in the calculations, because its effect on the haplogranite density is negligible (4.5 mass % B_2O_3 at 750 °C, 0.1 MPa, would decrease the haplogranite density by about 1 % according to Knoche *et al.*, 1992). Water solubility in NAS75:75 and NAS60:55 melts was estimated using an existing model based on experimental data in the Na_2O-Al_2O_3-SiO_2 system at 1100 °C and 0.8–2.0 GPa (Mysen, 2007), with water fugacity calculated using the Loner HGK solver (Haar et al., 1984), and the T dependence for similar compositions (Mysen and Wheeler, 2000). For MAC and HAPLO-B samples, an existing model for a granitic system at 800 °C and 0.3–0.7 GPa was used (Holtz *et al.*, 2001). The partial volume of water at high P and T in silicate melts was adopted from Malfait *et al.* (2014), measured for rhyolitic melts, but assumed to be independent of silicate melt composition, in agreement with Ochs and Lange (1999) and Bouhifd *et al.* (2015). At 700 °C and 0.2–1.5 GPa, a range of densities of 2.05–2.35 g/cm^3 for the four melt compositions was obtained. Overall, because the literature database at high P-T is incomplete, a 5 % error is assumed on the density estimate to account for possible deviations among different compositions not explicitly covered by the present models.

In the fluid phase, the determination of the density is more uncertain and requires knowledge of the composition of the fluid phase and corresponding equations of state. For sodium thiosulfate or sodium sulfate solutions, the solute concentration at the start of the experiment was precisely derived from cryometry measurements. At the high T of the experiment, some water dissolves in the melt, while some silicate melt dissolves in the aqueous fluid. Because our starting aqueous solutions are quite concentrated in salt (5–30 mass %), the effect of dissolved silicate is expected to be weak. Thus, the density of the fluid phase was approximated by that of the NaCl-H_2O system (Pokrovski *et al.*, 2009) at the same mass % NaCl concentration as that of the thiosulfate or sulfate solutions determined by cryometry, corrected for water dissolution in the melt, and using the T of homogenisation during heating and cooling of the fluid and assuming that the experimental cell volume was constant during the experiment (Table S-3). The estimated fluid densities at the experimental T and P are in the 0.9–1.2 g/cm^3 range with a typical uncertainty of ~10 % of the value.

1.4.4. Absorbance correction

Absorbance definition. The sulfur radical ions are chromophores, $S_3^{\bullet-}$ being blue and $S_2^{\bullet-}$ yellow (Chivers and Elder, 2013). This property is well known in ultramarine pigments, where $S_3^{\bullet-}$ and $S_2^{\bullet-}$ have been identified as responsible for blue and yellow-to-green colorations. The electronic absorption bands of $S_3^{\bullet-}$ and $S_2^{\bullet-}$ are centered at 600 nm and 390 nm respectively (Seel, 1984; Chivers and Elder, 2013). Similarly, aqueous solutions containing $S_3^{\bullet-}$ are blue when observed under the microscope (Fig. 1). With the 473 and 532 nm excitation lights, Raman bands of the two S radical species are thus enhanced (resonance Raman); this enhancement is stronger with the 532 nm laser than with the 473 nm laser for $S_3^{\bullet-}$ and the inverse for $S_2^{\bullet-}$ (Ledé *et al.*, 2007; Pokrovski and Dubessy, 2015). As the coloration increases, the laser light and the Raman scattering light are more and more absorbed by the solution, resulting in an apparent decrease of the intensity of the Raman spectrum, which is wavelength dependent (*i.e.* the signal absorption is greater for the species whose Raman band wavelengths are closer to the maximum of electronic absorption of the radical species; Schmidt and Seward, 2017). This effect is clearly observed for the most concentrated thiosulfate solutions (~3 molal) of the present study on the usually strong Raman band of water at ~3500 cm^{-1} that almost vanishes in those deep-blue solutions. As a result, the integrated intensities of the Raman bands of sulfur species in $S_3^{\bullet-}$-bearing fluids need to be corrected for this effect in order to obtain accurate fluid/melt partition coefficients. In the following, absorbance correction factors γ_i at the wavelength of the most intense Raman band of the i-th species with the λ_0 excitation are defined as:

$$I_{corr,abs,\omega_i} = \gamma_i \times I_{corr,\omega_i} \qquad \text{(Eq. S-3)}$$

where I_{corr,ω_i} is the intensity of the Raman band at the given Raman wavenumber ω_i (Eq. S-1) and I_{corr,abs,ω_i} is the theoretical intensity that would have the Raman band if the solution was not absorbing laser and Raman scattering lights.

Absorbance correction factor for O-H stretching band of water ($\gamma_{\nu OH}$). The effect of the absorption in colored solutions on the Raman band from O-H stretching vibrations of water is defined by the ratio of the molar scattering factor of water in the fluid phase at the temperature T of the experiment over that at ambient temperature at which the solution is fully transparent:

$$R_{\nu OH} = \frac{A^{20°C}_{\nu OH,\,fluid}}{A^{T}_{\nu OH,\,fluid}} \times \frac{V^{20°C}_{H_2O,\,fluid}}{V^{T}_{H_2O,\,fluid}} \tag{Eq. S-4}$$

where $A^{T}_{\nu OH,fluid}$ is the integrated intensity of the O-H stretching band at ~3500 cm^{-1} in the intensity-corrected Raman spectra acquired at the temperature T, and $V^{T}_{H_2O,fluid}$ is the partial molar volume of water at the temperature T and pressure P, calculated according to Driesner (2007). The values of $R_{\nu OH}$ are reported in Table S-3. In $S_3^{\bullet-}$-free experiments (GP6-8, GP13, GP15) the average $R_{\nu OH}$ value is 1.6 ± 0.4 (1 standard deviation, s.d.). This value is somewhat higher than the theoretical value of 1.0 likely due to changes in hydrogen bonds and the symmetry of the water molecules at high T, and the resulting proportion of water monomers and polymers that might have different Raman scattering cross-sections. The $R_{\nu OH}$ values in $S_3^{\bullet-}$-bearing fluids vary between 1.5 and 35.0, with the highest ones being found in the most S-concentrated fluids (Table S-3), clearly indicating that the OH stretching band of water in blue $S_3^{\bullet-}$-rich fluids is significantly absorbed. The absorbance correction factor $\gamma_{\nu OH}$ may be defined as the ratio between $R_{\nu OH}$ values in the colored fluid and in $S_3^{\bullet-}$-free solution:

$$\gamma_{\nu OH} \approx R_{\nu OH} \,/\, (1.6 \pm 0.8) \tag{Eq. S-5}$$

Estimation of the wavelength-dependent $S_3^{\bullet-}$ ion absorbance. The absorption correction for the Raman signal of sulfur species requires knowledge of the $S_3^{\bullet-}$ absorption envelope as a function of wavelength (Schmidt and Seward, 2017). The measurements of the absorption envelope were performed using a Bassett-type DAC installed at an Xplora Raman spectrometer equipped with a dispositive allowing light absorption measurements (CEMES, Toulouse) to quantify the absorbance of a 50 µm thick doubly polished section of a deep-blue crystal of natural lazurite from the American Museum of Natural History (sample n° 110457, courtesy of G. Harlow and J. Newman) mounted between the two diamond anvils. The DAC was illuminated from below with a white light, at the maximum intensity of the lamp, and a spectrum of the transmitted light was recorded for 0.2 s × 2, in the 400–800 nm range (spectrum I_1). Two 'blank' spectra were acquired: one without any sample between the two diamonds (spectrum I_0) and a second through a $S_3^{\bullet-}$-free sodalite sample mounted between the two diamonds (spectrum I_0'). The $S_3^{\bullet-}$-free sodalite was a powder of synthetic ultramarine pigment (courtesy of B. Ledé) heated for 4 days at 750 °C in air until it became colorless (all $S_3^{\bullet-}$ is oxidised to sulfate) and pressed between the two diamond anvils of the DAC to a thickness of a few µm. Because there was no significant difference between I_0 and I_0' spectra (*i.e.* $S_3^{\bullet-}$-free sodalite itself does not absorb), the absorbance (*Abs_ref*) of $S_3^{\bullet-}$ may be defined as follows

$$Abs\_ref = -\log_{10}\left(I_1 / I_0\right) \tag{Eq. S-6}$$

The absorption spectrum shows a maximum at ~600 nm (Fig. S-4) due to the $S_3^{\bullet-}$ ion well known in ultramarine pigments (Ledé *et al.*, 2007). There is also a low intensity absorption peak at ~450 nm, which might be the tail of the absorption band of $S_2^{\bullet-}$ or some other minor S species like polysulfides, which usually accompany $S_3^{\bullet-}$ both in natural and synthetic lazurites. This low intensity portion of the spectrum was ignored in the following treatment, since it is outside the range of Raman wavelengths acquired with 473 nm and 532 nm excitation. At 400 and 800 nm, measured absorbance is zero within the spectral noise, implying that refractive index corrections of $S_3^{\bullet-}$-bearing phases are negligible.

Calculation of absorbance correction factors γ_i of sulfur species. Combining the absorption correction factors of H_2O and the absorption spectrum of $S_3^{\bullet-}$ described above allows for estimation of the absorption correction factors of each species in the colored fluid phase. In the following analysis, we assume that the absorbance of the $S_3^{\bullet-}$-bearing fluids investigated in this study (*Abs*) follows the Beer-Lambert law:

$$Abs = \varepsilon \times C(S_3^{\bullet-}) \times l \tag{Eq. S-7}$$

where ε is the molar extinction coefficient of $S_3^{\bullet-}$ (mol^{-1}×cm^2), $C(S_3^{\bullet-})$ is the concentration of $S_3^{\bullet-}$ (mol×cm^{-3}), and l is the optical path defined by the distance (cm) between the two diamond anvils in the DAC. The laser light intensity is attenuated when it goes through the colored fluid to the focal point. The intensity of the Raman scattering is similarly attenuated when it goes from the focal point out of the fluid to the spectrometer. As a result, a double correction on Raman scattering intensities has to be applied:

$$\gamma_i = 10^{k\times Abs\_ref_0} \times 10^{k\times Abs\_ref_{\omega_i}} \tag{Eq. S-8}$$

where Abs_ref_0 is the absorbance of the reference lazurite at λ_0 and $Abs\_ref_{\omega_i}$ is the absorbance of the reference lazurite at the wavenumber ω_i of the Raman band of the species i, and k is a proportionality constant (*i.e.* the ratio of the fluid absorbance to the reference absorbance). For each $S_3^{\bullet-}$-bearing fluid in the present study, the k value was calculated with Eq. S-8, using the absorbance correction factors $\gamma_{\nu OH}$ from Eq. S-5. The resulting k values for $S_3^{\bullet-}$-bearing fluids vary between 0 and 1. Thus, Raman spectra can accurately be corrected for absorbance effect at any wavenumber shift based on Eq. S-8 and the obtained k value.

The γ_i values at the wavenumbers of each sulfur species and water bands, for k of 0.25, 0.5 and 1 (*i.e.* 3 different concentrations of the chromophore species $S_3^{\bullet-}$ that cover the range of the $S_3^{\bullet-}$-bearing aqueous fluids of the present study) for Raman spectra acquired with 473 and 532 nm excitation, are reported in Table S-4. Several observations can be made from these calculations. First, for a given concentration of $S_3^{\bullet-}$ chromophore, the decrease in the integrated intensity of the O-H stretching band due to $S_3^{\bullet-}$ absorbance is similar for both excitation wavelengths. Second, within our experimental range of $S_3^{\bullet-}$ concentrations, integrated intensities of Raman bands of sulfur species are almost unaffected by $S_3^{\bullet-}$ absorbance at 473 nm excitation, except the HS^-/H_2S band whose integrated intensity is reduced by up to a factor of ~4 in the most concentrated solution compared to an $S_3^{\bullet-}$-free fluid. Third, integrated intensities of Raman bands of sulfur species decrease by a factor similar to or higher than that of the water band with the 532 nm laser, and γ_i values are highly variable depending on the sulfur species; *e.g.*, the HS^-/H_2S integrated band intensity can be up to 5 times more affected than the integrated intensity of the O-H stretching band of water in the most concentrated solutions. Thus, the use of the 473 nm laser is a better choice for the determination of fluid/melt partition coefficients of sulfate, sulfide and $S_2^{\bullet-}$ species in $S_3^{\bullet-}$-bearing solutions, because errors associated with absorbance corrections are small even in the most concentrated thiosulfate solutions. However, the use of the 532 nm excitation light is advantageous to determine the fluid/melt partition coefficient of $S_3^{\bullet-}$ itself, because of the larger $S_3^{\bullet-}$ signal enhancement by the resonance phenomenon. Since the $S_3^{\bullet-}$ ion strongly partitions into the fluid, and has thus a very low abundance in the melt, it could only be detected in the melt if the 532 nm laser was used. In the $S_3^{\bullet-}$-rich experiments analysed with the 532 nm laser (GP1_a, GP15–GP17), the absorbance correction factor is similar for the O-H and $S_3^{\bullet-}$ bands. Due to the large variations of the $\gamma_{\nu OH}$ value (Table S-4) and the strong dependence of absorbance corrections on that value, absorbance corrections based on R values are very uncertain (*e.g.*, see values of $\gamma_{\nu OH}^*$ for GP1_b, GP16, and GP17 in Table S-4). Therefore, a different approach was applied for such S-rich solutions analysed using 532 nm excitation. The correction factors for Raman spectra of $S_3^{\bullet-}$-bearing solutions acquired with the 532 nm laser were adjusted to match the $D^{fl/mt}$ values obtained with the 473 nm laser in the same experiments. For $S_2^{\bullet-}$ and other S species for which the signal was below the detection limit with the 473 nm laser, this adjustment was made using the $D^{fl/mt}$ values obtained for SO_4^{2-}, H_2S/HS^- and H_2O species in $S_3^{\bullet-}$-poor experiments. This approach was applied to 3 experiments (GP1, GP16 and GP17, see footnote of Table S-3 for details). Note that for these experiments, the derived $S_3^{\bullet-}$ fluid/melt partition coefficients are minimum values; they might be higher if absorbance corrections are underestimated for these three concentrated solutions.

1.5. Error analysis

The major source of error on the fluid/melt partition coefficient values (Table S-5) stems from the determination of the integrated intensities of the Raman peaks of the sulfur species in the melt phase, being often close to the detection limit. For more abundant and thus clearly quantifiable sulfate and sulfide species in the melt (and for $S_3^{\bullet-}$ in few experiments), this source of error yields a factor of 2 for the Raman band integrated intensity value in the melt, whereas for $S_2^{\bullet-}$ and $S_3^{\bullet-}$ (in other experiments) only a minimum $D^{fl/mt}$ values could be determined. Another source of error is from the absorbance corrections in blue $S_3^{\bullet-}$-bearing solutions, based on the O-H stretching band of water and thus conditioned by the reproducibility of its intensity at high T in different experiments. The integrated intensity of the O-H stretching band is typically reproducible within 50 % of the value, yielding a rather small impact on the resulting absorption correction factors with 473 nm excitation (<10 % of γ_i value for the radical ions and sulfate and <30 % of γ_i value for sulfide), and a somewhat larger effect on spectra acquired with 532 nm excitation due to the stronger Raman signal absorbance (~50% of γ_i value). Additional smaller sources of uncertainties stem from the fluid and melt density estimations due to a lack of corresponding equations of state for our specific compositions, and uncertainties on the solute concentrations (alkalis, silica) due to partial dissolution of the melt in the fluid phase. However, phase densities usually evolve in a rather systematic and predictable fashion, so that our density assumptions are not expected to produce errors greater than 20 % of the final partition coefficient value. Uncertainties reported for $D^{fl/mt}$ coefficients obtained in this study are 1 s.d. (standard deviation) and estimated by combining the different sources of errors discussed above.

1.6. Estimation of sulfur radical ion concentrations in the fluid and melt phase from *in situ* experiments

Rough estimations of $S_3^{\bullet-}$ absolute concentrations in the aqueous fluid phase from our Raman spectra in $S_3^{\bullet-}$-bearing experiments can be made by using ratios of relative molar scattering factors of sulfur and water Raman bands published in the literature (Schmidt and Seward, 2017), coupled with the measured integrated intensities of S species Raman peaks and the spectral and absorption corrections applied in this study (section 1.4, Tables S-3 and S-4). Such estimations yield a range of absolute $S_3^{\bullet-}$ concentrations of ~5 to ~50% of total sulfur (*e.g.*, experiments GP17and GP1_b, respectively), for the 1-3 molal thiosulfate solutions at 700 °C and 0.3-1.5 GPa, employed in this study. Despite large variations, these estimates are within the range of $S_3^{\bullet-}$ values predicted in such solutions using the thermodynamic properties reported in Pokrovski and Dubessy (2015), as outlined in section 1.8 below. We, however, remain cautious about these spectroscopic estimations, since accurate quantification of each species concentration in such DAC experiments would require a different type of measurements employing tedious calibrations with standard solutions coupled with direct UV-Vis absorption measurements during high *T-P* experiments to properly correct for Raman signal absorption, in particular in the $S_3^{\bullet-}$-rich solutions evidenced in this study (*e.g.*, Fig. 1). Such measurements may be performed in near future with on-going improvements of our method. Note that the Raman peak ratios are much better constrained and allow far more accurate assessment of partition coefficients, which is the main strength of our novel approach. Similar rough estimates for species relative fractions made for the silicate melt phase in experiments where $S_3^{\bullet-}$ was detectable (*e.g.*, GP1_a, GP16) indicate radical ion fractions of 1 to 5 mol % of total S.

1.7. Derivation of total sulfur $D^{fl/mt}$ from *ex situ* experiments

The partitioning of S species measured *in situ* in this study was compared with that of total sulfur from a few quenched glass samples that could be recovered after the DAC experiments and with quench-based batch-reactor measurements on the same fluid-melt systems as those in DAC runs at 700 °C and 0.3 GPa. The conditions and system compositions of the batch-reactor experiments are reported in Table S-6. Gold capsules (3.9 mm inside diameter, 0.25 mm wall thickness, 10 mm length) were loaded with ~20 mg of glass powder and ~30 µL of sulfur-bearing solution, and sealed using an electric arc. Sealing was carefully checked by the absence of weight loss after heating the capsules at 110 °C for 0.5 h. The capsules were placed in cold-seal pressure vessels made of a Ni-based alloy (UDIMET-500, NiCr19Co18Mo4Ti3Al3), heated in horizontal furnaces and connected to a water pressure line (Jacquemet *et al.*, 2014). The alloy material of the vessel with water imposes redox conditions within ~1 log fO_2 unit of the nickel-nickel oxide buffer. The vessel was pressurised to 0.05 GPa at ambient temperature, then heated to 700 °C, and the final pressure was adjusted to 0.30 GPa. At the end of the experiment lasting from 1 to 10 days, the reactor was removed from the furnace, turned upside down to allow the capsule to fall in the colder part close to the reactor head (~300 °C), and cooled down in air stream, reaching T <100 °C in less than 10 min. Pressure was kept constant during the quench, by keeping the reactor connected to the pressure line. The retrieved gold capsules were weighed to check for eventual leaks and opened to recover the quenched silicate glass. Opening was always accompanied by the escape of the aqueous liquid phase and a typical H_2S smell. The glass was rinsed several times with distilled water to remove eventual sulfur and sulfate precipitates, and polished for microprobe and Raman analyses.

Analyses of quenched glasses both from hydrothermal reactor and DAC experiments by EPMA were performed at the University Paul Sabatier (Toulouse, France) using a Cameca SXFive microprobe. For S contents higher than 1000 ppm, the following operation conditions were applied: acceleration voltage 15 kV, beam current 10 nA, beam diameter 10 µm. All elements were measured for 10 s (5 × 2 s) on the peak and background. The short analysis duration and defocused beam were used to limit the Na migration during the beam exposure and avoid glass dehydration (Borisova et al., 2005). The following standards were used: albite (Na), wollastonite (Si, Ca), corundum (Al), sanidine (K), periclase (Mg), hematite (Fe) and celestine (S). The detection limit and the standard deviation for sulfur were ~300 ppm S. For S contents lower than 1000 ppm, the beam current was increased to 40 nA, Na was measured first for 3 s followed by S for 30 s. Both detection limit and standard deviation for S at these analytical conditions were ~80 ppm S. No S-bearing minerals were observed in the experimental products. The total S partition coefficient was calculated as the ratio of the fluid S concentration derived from mass balance to the S concentration measured in the silicate glass (Table S-7).

Raman analyses on few quenched glasses were performed at CEMES laboratory, using an Xplora spectrometer and 532 nm excitation wavelength. All glasses from batch-reactor and DAC experiments show only detectable sulfate species demonstrating that neither radical ions nor sulfide may accurately be preserved in quenched glasses, at least at our experimental conditions (see Section 2.2 for comparison with *in situ* data).

1.8. Thermodynamic predictions of sulfur speciation in the fluids used in this study

Sulfur speciation and radical ion concentrations may be estimated in the thiosulfate solutions used in this study, which are also a good proxy of the sulfur-rich fluids in subduction zones at the sulfide-sulfate transition, using the thermodynamic parameters of $S_3^{\bullet-}$ derived from extensive data at temperatures of <500 °C (see Pokrovski and Dubessy, 2015 for details and uncertainties). These parameters are based on the revised and extended HKF equation of state incorporating improved estimations of the dielectric constant of water at pressures to 6 GPa and temperatures to 1000 °C (Sverjensky *et al.*, 2014). Calculations were performed using the HCh computer code and associated databases, and based on the minimisation of the Gibbs free energy of the system and accounting for non-ideality of aqueous saline solution using the extended Debye-Hückel model (Shvarov, 2008, 2015). The calculations indicate that, along with sulfate and sulfide species, $S_3^{\bullet-}$ is a dominant redox form and may account for as much as 50% of total dissolved sulfur in the fluids of this study at 700 °C and 0.5-1.5 GPa (Fig. S-8). These predictions are in agreement with direct estimations of absolute concentrations of $S_3^{\bullet-}$ from the Raman signal (Section 1.6). At present, we cannot predict the $S_2^{\bullet-}$ contents at these conditions, because the stability constants for this ion are currently available only at 450 °C and pressures <0.15 GPa (Pokrovski *et al*., 2019), and thus cannot be reliably extrapolated to the much higher *T*-*P* of this study. Note that in the presence of silicate melts, the abundances of both radical ions may be significantly affected compared to the melt-free thiosulfate solution, with low-alkalinity melts (HAPLO-B, MAC) imposing more acidic fluid pH further increasing the $S_3^{\bullet-}$ abundance compared to that shown in Fig. S-8, and with more alkaline melts (NAS 75:75 and 60:55) imposing more basic pH and, consequently, favouring $S_2^{\bullet-}$ formation (see Eqs. 1 and 2 in the main text).

2. Supplementary Text: Additional Notes

2.1. Overview of the strengths and limitations of the existing *ex situ* measurements of S fluid/melt partitioning versus the *in situ* method developed in this study

Most *ex situ* data on bulk sulfur fluid/melt partitioning published in the literature have been mostly obtained by measuring the total sulfur content in the quench silicate glass after the experiment with electron microprobe. Usually, the fluid phase is not recovered and its sulfur content is estimated by mass balance difference between the initially loaded S amount, the S amount contained in the quenched glass and the S amount eventually contained in crystals (if present). This approach usually gives reliable data with a standard deviation of 10-50 %. The major limitations are the following: 1) the estimation of the volume of sulfur-bearing crystals in the melt, in some studies, might potentially have large uncertainties because of their inhomogeneous nucleation and distribution in the glass; 2) the large sensitivity of the $D^{fl/mt}$ values to eventual losses of sulfur during the experiment (for instance to the capsule made of metals other than gold or of gold alloys with metals easily forming sulfides like Cu, Pd, Ag, Fe); 3) the limited pressure range that can be attained in most studies (typically <0.5 GPa, Table S-8), except few studies that were conducted at pressures of 2-3 GPa (*e.g.*, D'Souza and Canil, 2018; Jégo and Dasgupta 2013, 2014), but in those high-*P* works the question arises of whether the volatile species are quenchable in the highly hydrated glass; and 4) the impossibility to determine the sulfur speciation in the fluid (and in most cases in the melt) for better interpretation of bulk S partition coefficients, becausee some of the high *T*-*P* sulfur species are not quenchable (e.g., SO_2, radical ions, polysulfides, molecular sulfur; Pokrovski and Dubessy, 2015; Kokh *et al*., 2020).

In situ data were obtained in this study by measuring simultaneously by Raman spectroscopy the signal of each individual S species in both melt and fluid phase directly at elevated *T*-*P* conditions. This method has the advantage of 1) allowing direct *in situ* observation of what happens in the experiment (melting, nucleation, crystallisation); 2) directly investigating sulfur chemical speciation; 3) enabling rapid attainment of equilibrium (<minutes) due to the small experimental chamber volume (~10^6 times smaller than the volumes of capsules/containers commonly used in most *ex situ* experiments) and efficient convection; 4) being much less sensitive to eventual loss of sulfur during the experiment and to the presence of S-bearing crystalline phases (that may easily be identified optically and detected by Raman spectroscopy); 5) allowing measurements across a larger *P*-range (from P_{sat} to several GPa) pertinent to magma generation and evolution in subduction zones; and 6) avoiding the pitfalls of quench effects particularly significant in high-pressure (> 0.4 GPa) experiments involving hydrous melts. The current limitations of our *in situ* method are the following: 1) quantitative Raman analysis requires several corrections, in particular for light absorption by strongly colored sulfur radical species (*e.g.*, see Section 1.4.4); 2) run durations are currently limited to several hours and temperatures of <750 °C due to degradation of heating elements and diamonds at higher temperatures; 3) the difficulties to recover the quenched phases after the run due to the intrinsically small DAC volume; 4) the difficulties to accurately buffer or impose the desired redox conditions; and 5) lower accuracy for pressure determination in single-phase systems than that for large-volume reactors used in *ex situ* studies. Future developments of the DAC setup (*e.g.*, laser heating, gasketless designs) will allow the actual temperature range to be largely extended offering possibilities to study silicate melts of mafic to ultramafic compositions (*i.e.* with liquidus temperatures of >1000 °C).

2.2. Comparison of *in situ* with *ex situ* data on sulfur fluid-melt partition coefficients

Our first *in situ* data on S species partitioning in fluid-melt systems may be compared with *ex situ* data on bulk sulfur distribution obtained from quenched products in this and previous work on intermediate to felsic melts.

Because the fluid phase is partly lost upon the experiment termination, $D^{fl/mt}(S_{tot})$ values in *ex situ* studies were retrieved from total S concentrations analysed in quenched silicate glasses and using sulfur mass balance with the initially loaded S. The $D^{fl/mt}(S_{tot})$ values, estimated using this approach, for a few glasses that could be recovered after DAC experiments of this study (Table S-7), are more than a factor of 10 higher than those measured *in situ* for sulfate and sulfide in these DAC experiments (Table S-5 and Figure S-5). Even though these data are subject to significant uncertainties, they point to the major potential pitfall of the *ex situ* approach related to (partial) loss of sulfur from melt during the quench, at least at the high pressures investigated here (>0.5 GPa).

To better evaluate the advantages and limitations of our novel *in situ* method, we also have performed a small series of experiments on the same fluid-melt systems as those in the *in situ* DAC measurements using quench-based batch reactors (section 1.7). The derived $D^{fl/mt}$ values for total sulfur (S_{tot}) (Tables S-6, S-7) display a significant variability, spanning from ~20 to 200 at 700 °C and 0.3 GPa in the systems with NAS75:75 and HAPLO-B melts and a thiosulfate solution. This variability is likely due to large changes in sulfur speciation and, in particular, in radical ion concentrations in the fluid in response to small changes in oxygen fugacity across the sulfate-sulfide transition in the reactors through time (*e.g.*, run HTM4 *vs* HTM9, lasting <1 and 6 days, respectively, Table S-6). Other factors that possibly contribute to the variability of our *ex situ* batch-reactor data are changes in melt composition (alkalinity) during the run. For example, the $D^{fl/mt}(S_{tot})$ value is the lowest in an experiment where the final quenched glass is the most peralkaline (run HTM2, Table S-7), which is also consistent with known alkalinity trends (*e.g.*, Zajacz, 2015).

Our *in situ* partitioning data on sulfate and sulfide may further be compared with numerous available literature data on bulk $D^{fl/mt}(S_{tot})$ values for felsic and 'intermediate' melt compositions from *ex situ* experiments performed at redox conditions corresponding to the domains of predominance of sulfide (generally <NNO) and sulfate (generally >NNO+2), depending on *T*-*P* and melt composition (Fig. S-5 and S-6, Table S-8). Even though our own *in situ* data at redox conditions beyond the sulfide-sulfate boundary (<NNO to >NNO+2, Fig. S-5) are rather scarce, such a comparison is allowed because the partition coefficient of a given sulfur redox form (sulfate or sulfide) is independent of oxygen fugacity. In contrast, they are expected to be dependent on alkalinity, since the exact speciation of sulfate (SO_4^{2-}, HSO_4^-, and their alkali ion pairs) and sulfide (H_2S, HS^- and its alkali ion pairs) strongly depends both on pH and alkali content of the system. The *in situ* values ($D^{fl/mt}$ ~ 6–34; Table S-5) obtained in this study are situated in the lower part of the large range of values (from <1 to >2000) reported in the literature at *T* of 750–1300 °C and *P* of <0.5 GPa over a wide range of alkalinity. The fact that *ex situ* studies indicate higher $D^{fl/mt}$ values may be the result of more contrasting properties (*i.e.* density, viscosity, dielectric constant and hydration extent) between melt and fluid favouring sulfur partitioning into the more volatile, water-rich and less dense fluid phase at the higher-*T* and lower-*P* conditions covered by those *ex situ* studies. Furthermore, the sensitivity of $D^{fl/mt}(S_{tot})$ values to the melt alkalinity is expected to be amplified at such more contrasting fluid-*vs*-melt properties compared to our measurements. Some available literature data show $D^{fl/mt}(S_{tot})$ values decreasing with increasing melt alkalinity in the redox domain of sulfate predominance (Zajacz *et al.*, 2012, 2013; Zajacz, 2015; Masotta *et al.*, 2016; Binder *et al.*, 2018), whereas others (*e.g.*, Scaillet and Macdonald, 2006) do not confirm such trends (Fig. S-6). These discrepancies may partly be related to the presence of SO_2 in the fluid phase, in addition to sulfate, in some of those works (SO_2 being far more volatile than SO_4^{2-} and its ion pairs). Furthermore, in the vicinity of the sulfate-sulfide redox transition, interpretation of *ex situ* data is complicated by large changes in S speciation, over a narrow range of fO_2, from sulfide to $S_3^{\bullet-}$ and $S_2^{\bullet-}$ and to sulfate (NNO to NNO+2; Fig. 4). Our study reveals, for the first time, that the radical ions, inaccessible by *ex situ* approaches, may also contribute to the large variability of existing $D^{fl/mt}(S_{tot})$ values (Fig. S-5). Thus, our data highlight the importance of knowing, when interpreting bulk S partitioning trends, detailed S speciation in the fluid, which may only be directly assessed via *in situ* measurements.

Furthermore, our *in situ* data may offer direct insight into sulfide speciation in the fluid and melt phase, with HS^- (and its ion pairs with alkali ions, Na^+ and K^+) being favoured at the expense of H_2S in more alkaline fluids, leading to somewhat more elevated $D^{fl/mt}$(sulfide) values with increasing alkalinity (Fig. 3), at least at the relatively low T (700 °C) and high P (>0.2 GPa) conditions covered by our measurements. Even though our *in situ* data are at present quite limited, they point to potentially large changes in S speciation in the fluid phase with T and P that may result in opposite changes in $D^{fl/mt}$ values. For example, the presence of high NaCl concentrations (60 mass %) in the fluid was shown to lead to a strong decrease of $D^{fl/mt}$(sulfide) in a haplogranite system at 850 °C and 0.2 GPa (Binder et al., 2018), which was interpreted by the growing fraction of the NaHS ion pair at the expense of the more volatile H_2S in the fluid with increasing Na content. Our *in situ* data acquired at 700 °C and 0.3-1.5 GPa show a weak opposite trend for $D^{fl/mt}$(sulfide) values with Na content of the fluid (proportional to alkalinity, Fig. 3), which does not confirm such an interpretation. Note that the initial range of alkalinity in our experiments, plotted in this figure, may be larger compared to equilibrium melt compositions due to enhanced solubility of Na in the fluid (Table S-7). Therefore, more accurate evaluation of alkalinity trends would require detailed investigations at different specific compositions. Indeed, variations of S species exact distribution within the same S redox form (e.g., SO_4^{2-}, HSO_4^-, $NaSO_4^-$) as a function of melt and fluid compositions (especially in a large range of alkalinity) may have a significant effect on the total S melt/fluid partition coefficient (*e.g.*, Zajacz, 2015), in some cases comparable to the effect of variations between the abundance of the different S redox forms (sulfate, sulfide and radical ions) of very contrasting volatile properties.

Finally, our *in situ* data may be compared with the few existing *ex situ* measurements of sulfur partitioning using quench-based methods at higher P (2–3 GPa) and T (800–1050 °C) in aqueous fluid-rhyolite melt systems produced by partial melting of pelite and basalt (Jégo and Dasgupta, 2013, 2014; D'Souza and Canil, 2018; Table S-8). Remarkably, our *in situ* $D^{fl/mt}$ values of sulfide and sulfate are lower, by at least a factor of 10 to 100, than those measured *ex situ* in these studies. This systematic discrepancy likely reflects the difficulty to quench high-pressure hydrous melts (>10 mass% H_2O) relevant to deep magma generation in subduction zones, compared to silicate melts at lower pressures (<0.5 GPa) which are easier to quench in *ex situ* experiments (see above). Our study highlights the necessity for *in situ* methods to obtain robust partitioning data in fluid-melt systems at depth.

3. Supplementary Tables

Table S-1 Starting compositions in mass % of the silicate glasses investigated in this study.

Sample	MAC[(a)]	HAPLO-B[(b)]	NAS 60:55[(c)]	NAS 75:75
SiO_2	72.4±0.5	75.3±0.4	50.9±0.4	71.4±0.5
Al_2O_3	15.8±0.2	11.7±0.2	26.4±0.2	10.1±0.2
Na_2O	3.7±0.6	4.7±0.2	20.6±0.2	18.5±0.5
K_2O	3.7±0.1	4.0±0.1		
B_2O_3	0.6	4.2±0.2*		
F	1.6±0.2			
FeO	0.6±0.1			
P_2O_5	0.6±0.1			
Total	98.8	100.0	97.9	100.0
Alkalinity[(d)]	0.6	1.1	1.3	3.0
Natural rock equivalent	rhyolite	haplogranite	phonolite	peralkaline rhyolite

(a) ICP-AES as reported in Borisova *et al.* (2010).
(b) EPMA analyses, this study (CAMECA SXFive, 15 keV, 10 nA, beam size 10 µm, 3 s per element).
(c) EPMA analyses as reported in Toplis *et al.* (1997); all errors are 1 s.d.
(d) Alkalinity = (Na + K) / Al (mol/mol).
* B_2O_3 content was calculated as the difference between 100 % and total mass % determined by EPMA.

Table S-2 Experimental conditions of the DAC experiments and detected S species in each phase.

Run	Solution	Molality (±0.1)	$S_{tot,fl}$(b) (±0.1) mass %	λ_0 nm	*P*(c) (±0.1) GPa	*T* (±2) °C	Observed species in the fluid	Observed species in the melt
MAC								
GP3	$Na_2S_2O_3$	3.1	13.3	473	1.0	700	$S_3^{\bullet-}$, $S_2^{\bullet-}$, SO_4^{2-}, H_2S/HS^-, H_2O	SO_4^{2-}, H_2S/HS^-, H_2O
GP4	$Na_2S_2O_3$	0.6	3.5	473	1.3	700	$S_3^{\bullet-}$, $S_2^{\bullet-}$, SO_4^{2-}, H_2S/HS^-, H_2O	H_2O
GP9	$Na_2S_2O_3$	3.5	14.4	473	0.3	700	$S_3^{\bullet-}$, $S_2^{\bullet-}$, SO_4^{2-}, H_2S/HS^-, H_2O	SO_4^{2-}, H_2O
GP10	H_2SO_4	0.9	2.7	473	1.5	700	None; crystals cover the entire cell	
GP11	H_2SO_4	3.4	8.2	473	1.4	700	SO_4^{2-}, H_2SO_4, SO_2, H_2O	None; melt sticks to the bottom of the cell
HAPLO-B								
GP15(a)	Na_2SO_4	3.2	7.1	532	0.3	700	SO_4^{2-}, H_2O	SO_4^{2-}, H_2O
GP16(a)	$Na_2S_2O_3$	3.0	13.0	532	0.6	700	$S_3^{\bullet-}$, SO_4^{2-}, HS^-, H_2O	$S_3^{\bullet-}$, H_2O
GP17(a)	$Na_2S_2O_3$	0.8	4.6	532	0.8	700	$S_3^{\bullet-}$, SO_4^{2-}, H_2S/HS^-, H_2O	H_2O
NAS60:55								
GP6	$Na_2S_2O_3 + C_xH_y$	1.4	7.4	473	0.4*	700	HS^-, CH_4, H_2O	HS^-, CH_4, H_2O
GP7	$Na_2S_2O_3$	0.4	2.4	473	0.7*	700	SO_4^{2-}, HS^-, H_2O	SO_4^{2-}, H_2O
GP8	$Na_2S_2O_3$	0.6	3.5	473	0.7	700	SO_4^{2-}, HS^-, H_2O	SO_4^{2-}, HS^- (e)
GP13	Na_2SO_4	1.0	2.8	473	1.1	700	SO_4^{2-}, HS^-, H_2O(f)	H_2O
GP13	Na_2SO_4	1.0	2.8	473	0.8	700	SO_4^{2-}, HS^-, H_2O(f)	H_2O
NAS75:75								
GP1_a	$Na_2S_2O_3$	1.9	9.4	532	0.8*	700	$S_3^{\bullet-}$, SO_4^{2-}, HS^-, H_2O	$S_3^{\bullet-}$, SO_4^{2-}, HS^-, H_2O
GP1_b(a)	$Na_2S_2O_3$	1.9	9.4	473	0.8*	700	$S_3^{\bullet-}$, $S_2^{\bullet-}$, SO_4^{2-}, HS^-, H_2O	SO_4^{2-}, HS^-, H_2O

(a) The quenched glass was recovered for *ex situ* EPMA analyses.

(b) Concentration of sulfur in the loaded solution determined by cryometry.

(c) Determined from Raman spectra of zircon, unless specified as *, that means estimated from EoS of NaCl-H_2O solution (Driesner, 2007) of equivalent solute content (mass %) and from homogenisation temperature of the fluid.

(d) For simplification, bands corresponding to silicate and boron dissolved in the fluid are not reported. The term 'sulfide' is used when it was not possible to distinguish between HS^- and H_2S based on the wavenumber shift.

(e) Sulfate melt present.

(f) The presence of HS^- bands of low intensity in experiments in which sulfur was loaded as sulfate, could be due to a contamination during the loading of the silicate glass or S-bearing solution; since the samples are so tiny, any trace of remaining glue or plastic from the sample container might contribute to the reduction of a small fraction of sulfate. In addition, reactions with the diamond windows or diffusion of the surrounding gas (Ar + H_2) would also reduce sulfate. However, this reduction has no impact on fluid/melt partition coefficients, because we identify and measure each individual species independently, using our *in situ* method.

Table S-3 Values of correction factors used in this study to calculate $D^{fl/mt}$ partition coefficients from *in situ* experiments at 700 °C.

Run	d_{melt}(a) (±0.05) g.cm^{-3}	d_{fluid}(a) (±0.1) g.cm^{-3}	**Total dissolved load (±1) mass %**	λ_0 nm	R_{vOH} (b)	γ_{vOH} *(c) (±50 %)	γ_i **applied in this study**(d)				
							$\gamma\ S_2^{\bullet-}$ 585 cm^{-1}	$\gamma\ S_3^{\bullet-}$ 532 cm^{-1}	$\gamma\ SO_4^{2-}$ 980 cm^{-1}	$\gamma\ H_2S/HS^-$ 2585 cm^{-1}	γ_{vOH} 3500 cm^{-1}
MAC											
GP3	2.12	1.23	42	473	12.8	8	1.2±0.1	1.2±0.1	1.3±0.1	2.9±0.8	8±4
GP4	2.06	1.10	15	473	2.5	1.6	1	1	1.1±0.1	1.3±0.3	1.6±0.8
GP9	2.16	0.96	39	473	22.2	14	1.2±0.1	1.2±0.1	1.3±0.1	3.8±1	14±7
HAPLO-B											
GP15	2.13	1.04	39	532	*3.6*		1	1	1	1	1
GP16	2.12	1.14	40	532	35.0	22(e)	6.1±0.4	5.8±0.4	9.0±0.7	16.3±1.7	7.1±0.5
GP17	2.11	0.97	15	532	2.9	1.9(f)	1	1	1	1	1
NAS60:55											
GP6	2.23	0.89	21	473	*1.6*		1	1	1	1	1
GP7	2.29	0.92	6	473	*1.3*		1	1	1	1	1
GP13	2.35	1.06	15	473	*1.9*		1	1	1	1	1
GP13	2.31	0.97	15	473	*2.1*		1	1	1	1	1
NAS75:75											
GP1_a	2.21	1.09	28	532	4.8	3.1(g)	1.5±0.1	1.4±0.1	1.6±0.1	1.8±0.2	1.5±0.1
GP1_b	2.21	1.05	27	473	1.5	1.0	1	1	1	1	1

(a) d_{melt} and d_{fluid} are the calculated densities of the melt and the fluid at the temperature of the experiment (Section 1.4.3).

(b) R_{vOH} is the ratio of the molar scattering factor of water in the fluid phase at given T over that at ambient temperature; R_{vOH} values for $S_3^{\bullet-}$-free experiments are in italic.

(c) $\gamma_{vOH}{}^*$ is the theoretical value of the absorbance correction factor calculated based on R values (see Section 1.4).

(d) For experiments GP16, GP17 and GP1, γ_i values applied to obtain sulfur partition coefficients are not calculated based on $\gamma_{vOH}{}^*$ (see notes (e), (f) and (g) below).

(e) Applying this absorbance correction would give $D^{fl/mt}(H_2O)$ = 18±10 compared with the value of 6±1 obtained in GP17 (same silicate melt HAPLO-B, but lower $S_3^{\bullet-}$ content) at similar P (0.6 and 0.8 GPa, respectively). Therefore, γ_{vOH} was adjusted to get the similar $D^{fl/mt}(H_2O)$ value for the two experiments, and the corresponding γ_i for the sulfur species were calculated using Eq. S-8.

(f) Within uncertainties it was impossible to determine if the presence of $S_3^{\bullet-}$ has a significant effect on the integrated intensity of the O-H stretching band of water. In addition, the intensities of the $S_3^{\bullet-}$ and H_2S Raman bands in the fluid decreased by a factor of 4 between two spectra acquired at 700 °C and 2 h of interval, probably due to sulfur reaction with the iridium gasket. However, the integrated intensity of the O-H stretching band of water remained unchanged between the two fluid Raman spectra. Thus, we assumed $\gamma_{vOH} = 1$.

(g) The value of γ_{vOH} at 532 nm excitation was adjusted to match the value of $D^{fl/mt}(H_2O)$ obtained at 473 nm excitation; this value was used to calculate γ_i for the sulfur species using Eq. S-8.

Table S-4 Values of the absorbance correction factors γ_i at the indicated wavenumbers for 3 different absorbances of $S_3^{\bullet-}$ and the two excitation lights (λ_0) used in this study.

$k^{(a)}$	λ_0=473 nm				λ_0=532 nm			
	$\gamma\ S_3^{\bullet-}$ 532 cm^{-1}	$\gamma\ SO_4^{2-}$ 980 cm^{-1}	$\gamma\ H_2S/HS^-$ 2585 cm^{-1}	γvOH 3500 cm^{-1}	$\gamma\ S_3^{\bullet-}$ 532 cm^{-1}	$\gamma\ SO_4^{2-}$ 980 cm^{-1}	$\gamma\ H_2S/HS^-$ 2585 cm^{-1}	γvOH 3500 cm^{-1}
0.25	1.0	1.1	1.4	2.0	2.0	2.3	2.9	2.1
0.5	1.1	1.2	2.0	3.9	3.8	5.4	8.4	4.5
1	1.2	1.4	3.9	15.1	14.7	28.7	70.7	19.9

(a) *k* is the ratio between the absorbance of the $S_3^{\bullet-}$-bearing solution and that of a reference blue lazurite (AMNH).

Table S-5 Fluid/melt partition coefficients calculated in this study for individual sulfur redox forms at specified *T-P* conditions (errors 1 s.d.).

Run$^{(a)}$	$S_{tot,fl}$$^{(b)}$ mass %	*T* ° C	*P* GPa	$D^{fl/mt}(S_2^{\bullet-})^{(c)}$	$D^{fl/mt}(S_3^{\bullet-})^{(d)}$	$D^{fl/mt}$(sulfate)	$D^{fl/mt}$(sulfide)
MAC							
GP3	13.3	700	1.0	>45	>50	6±2	6±2
GP4	3.5	700	1.3	>40	>85	>27	>8
GP9	14.4	700	0.3	>10	>45	14±7	
HAPLO-B							
GP15$^{(a)}$	7.1	700	0.3			9±5	
GP16$^{(a)}$	13.0	700	0.6		155 (100–450)	>25	
GP17$^{(a)}$	4.6	700	0.8		>380	>40	>12
NAS 60:55							
GP6	7.4	700	0.4				33±17
GP7	2.4	700	0.7			31±18	18±9
GP13	2.8	700	1.1			16±5	
		700	0.8			18±9	
NAS75:75							
GP1_a	9.4	700	0.8		150 (80–320)	24±3	34±15
GP1_b$^{(a)}$	9.4	700	0.8	>70	>20	18±3	31±8

(a) The quench glass was recovered for *ex situ* EPMA analysis.
(b) Concentration of sulfur in the loaded solution determined by cryometry.
(c) Only minimum values are given for $S_2^{\bullet-}$ as this species was not detected in the melt.
(d) When error bars are not symmetric, because S species is close to detection limit in the melt, minimum and maximum values are also given in parentheses: ($D^{fl/mt}$min–$D^{fl/mt}$max).

Table S-6 Conditions of batch-reactor experiments for bulk sulfur $D^{fl/mt}$ determination.

Run	Glass loaded	Solution loaded	Molality	$S_{tot,fl}$(a) mass %	T °C	P GPa	Glass:Fluid mass ratio	Duration (day)
HTM2	NAS75:75	$K_2S_2O_3$	1.0	5.4	700	0.31 0.30	1.0:1.0	7
HTM4	NAS75:75	$Na_2S_2O_3$	2.0	9.7	700	0.31	1.0:1.9	0.8
HTM9	NAS75:75	$Na_2S_2O_3$	2.0	9.7	700	0.31	1.0:1.8	6
HTM8	HAPLO-B	$Na_2S_2O_3$; $K_2S_2O_3$	0.60; 0.30	5.3	700	0.31	1.0:1.7	4

(a) Concentration of sulfur in the loaded solution.

Table S-7 Electron probe microanalyses (EPMA) of quenched glasses (batch reactor experiments and DAC experiments) and calculated bulk sulfur partition coefficient (error 1 s.d.).

Run	$S_{tot,fl}$(a) mass %	nb pts(b)	SiO_2-Al_2O_3-Na_2O-K_2O composition(c)				H_2O +B_2O_3(c)	$S_{tot,melt}$ μg/g	$D^{fl/mt}(S_{tot})$
			SiO_2	Al_2O_3	Na_2O	K_2O			
HAPLO-B									
GP17	4.6	10	78.9±0.6	12.4±0.3	5.2±0.3	3.5±0.1	13.1±0.3	89±31	680±240
GP15	7.1	12	77.5±2.3	12.4±1.2	6.3±0.8	3.9±0.5	13.8±0.8	170±25	520±80
GP16	13.0	15	80.9±2.4	11.3±0.9	4.9±0.3	2.9±0.5	11.7±0.9	478±25	340±25
HTM8	5.3	19	77.9±0.9	12.9±0.8	3.8±0.2	5.4±0.9	10.8±1.5	297±89(e)	200±70
NAS75:75									
GP1_b	9.4	13	81.1±1.2	8.9±0.8	9±0.7	1.0±0.1	11.4±0.9	720±160	160±40
HTM2	5.4	6	72.4±0.9	10.9±0.2	8.6±0.8	8.1±1.1	12.8±0.8	2429±374	23±4
HTM4	9.7	51	79.4±1.8	11.2±1.8	9.3±0.6	-	12.3±1.8	1000±315	102±33
HTM9	9.7	9	80.3±0.7	11.4±0.2	8.3±0.2	-	11.8±0.7	542±36(f)	189±16

(a) Concentration of sulfur in the loaded solution (as determined by cryometry in the DAC experiments labelled ‘GP’).
(b) Number of EPMA analyses for major elements.
(c) Normalised to 100 mass % of EPMA analyses.
(d) Deduced from difference to 100 mass %.
(e) Number of EPMA analyses for sulfur = 48.
(f) Number of EPMA analyses for sulfur =19.

Table S-8 Compilation of *ex situ* data on bulk sulfur fluid/melt partitioning obtained from quenched products in previous work on felsic and intermediate melts (shown in Fig. S-5 and S-6) and the corresponding experimental conditions.

Type of glass investigated, reference Run name *(type of partial melt)*	P **GPa**	T **°C**	**log(f_{O_2}) (ΔNNO)**	**Melt alkalinity(a)**	**SiO$_2$ mass %(b)**	$D^{fl/mt}$(S$_{tot}$)	**1 s.d.(c)**
White dacite, Scaillet *et al.* (1998)							
17	0.22	776	-0.01	0.6	75.9	1	
19	0.22	776	1.04	0.6	76.2	6	
21	0.23	776	1.71	0.6	77.1	689	
42b	0.23	899	1.20	0.6	68.8	72	
52	0.22	781	2.27	0.6	75.4	691	
53	0.22	781	2.27	0.6	77.6	921	
58	0.22	781	2.27	0.6	76.6	1564	
69	0.40	780	2.63	0.6	74.6	729	
75J	0.22	778	1.40	0.6	79.2	1310	
Haplogranite, Keppler (2010)							
	0.20	850	0.5	1.0	80.3	47	4
	0.20	850	-1.5	1.0	80.1	468	32
	0.30	850	0.5	1.1	80.3	68	5
	0.20	850	0.5	1.1	80.3	47	4
	0.10	850	0.5	1.0	80.4	94	9
	0.05	850	0.5	1.0	80.7	58	3
	0.30	750	0.5	1.1	80.0	137	7
	0.20	750	0.5	1.1	80.0	51	2
	0.20	850	4.4	1.1	80.3	49	2
Rhyodacite, Botcharnikov *et al.* (2004)							
S100-S102	0.20	850	0	0.7	70.1	1430	400
Phonolite, Webster *et al.* (2009)							
1-02-28a	0.20	1022	nr(l)	1.6	55.4	93	
1-02-21a	0.20	992	nr	1.7	58.1	339	
1-03-02a	0.20	984	nr	1.6	60.5	2	
1-02-21b	0.20	1000	1.19	1.7	59.2	69	
1-02-44b	0.20	991	1.19	1.7	60.5	12	
1-02-44c	0.20	991	1.63	1.6	60.4	47	
1-02-45a	0.20	998	1.00	1.7	59.9	41	
1-02-45b	0.20	998	1.10	1.7	59.6	47	
1-03-02b	0.20	984	1.16	1.7	60.0	45	
1-04-07b	0.20	927	0.99	1.7	59.2	54	
1-04-07c	0.20	927	1.44	1.8	61.0	128	
1-04-08a	0.20	927	1.50	1.8	59.3	89	
1-04-08b	0.20	927	1.56	1.8	61.3	46	
1-04-08c	0.20	927	0.79	1.8	62.3	133	
1-05-16a	0.20	925	0.88	1.7	62.7	155	
1-05-16b	0.20	925	0.75	2.0	64.0	168	
1-05-16c	0.20	925	0.99	1.8	61.0	134	
1-05-17	0.20	920	0.67	2.0	61.9	232	
1-05-18a	0.20	920	nr	1.8	61.1	282	
1-05-18b	0.20	920	1.12	1.8	63.5	155	
1-05-18c	0.20	920	nr	1.8	63.3	271	
1-05-19a	0.20	920	nr	2.0	62.1	745	
1-05-19b	0.20	920	0.80	1.7	61.1	66	
1-05-20a	0.20	920	0.69	2.0	64.2	285	
1-05-20b	0.20	920	nr	2.0	60.0	364	
1-05-20c	0.20	920	0.54	2.0	60.8	271	
1-05-21a	0.20	920	0.99	1.8	61.7	263	
1-05-21b	0.20	920	0.76	1.9	63.2	214	
1-05-21c	0.20	920	0.62	2.0	64.4	277	
1-05-23	0.20	920	0.76	2.0	62.1	146	
1-05-24a	0.20	920	nr	1.9	63.4	176	
1-05-24c	0.20	920	0.86	1.9	64.0	189	

Table S-8 continued

Type of glass investigated, reference Run name *(type of partial melt)*	***P*** **GPa**	***T*** **°C**	**log(f_{O_2})** **(ΔNNO)**	**Melt alkalinity(a)**	**SiO_2** **mass %(b)**	**$D^{fl/mt}$(S_{tot})**	**1 s.d.(c)**
1-05-25	0.20	915	0.80	1.8	62.5	169	
1-06-01	0.20	915	0.97	1.7	62.4	62	
1-06-02	0.20	898	nr	1.6	58.8	258	
1-06-03	0.20	905	0.54	1.7	60.8	162	
1-06-04	0.20	910	1.08	1.7	61.3	169	
1-06-05	0.20	896	nr	1.7	58.3	983	
1-06-07	0.20	908	1.19	1.7	60.1	1096	
1-06-08	0.20	904	0.60	1.6	57.3	172	
Haplogranite, Webster *et al.* (2011)							
1-08-03A	0.20	900	0.89	1.0	78.0	278	
1-08-03B	0.20	900	0.37	1.0	77.8	185	
1-08-03C	0.20	900	0.15	1.1	76.8	266	
1-08-04A	0.20	900	nr	1.0	77.3	149	
1-08-04B	0.20	900	nr	1.0	77.1	153	
1-08-04C	0.20	900	0.69	1.0	76.4	359	
1-08-05B	0.20	900	0.33	1.0	77.3	226	
1-08-05C	0.20	900	0.51	1.0	77.6	195	
1-08-06B	0.20	909	0.11	1.0	77.5	169	
1-08-06C	0.20	909	0.51	1.0	77.7	121	
1-08-07A	0.20	897	1.45	1.0	77.6	67	
1-08-07B	0.20	897	0.48	1.0	77.3	50	
1-08-07C	0.20	897	0.38	1.0	77.5	59	
1-08-12	0.20	905	0.26	1.0	77.4	271	
1-08-14A	0.20	895	0.51	1.0	77.9	161	
1-08-14B	0.20	895	0.63	1.0	77.4	156	
1-10-02A	0.20	899	-0.39	1.0	77.3	311	
1-10-02B	0.20	899	0.53	1.0	77.4	162	
Peralkaline rhyolite, Scaillet and Macdonald (2006)							
ND-1, ND-9	0.15	852	-1.62	1.1	77.1	301	
ND-2, ND-4	0.15	804	0.33	1.0	77.2	276	
ND-3, ND-5, ND-6	0.15	806	2.19	1.0	77.4	223	
SMN-1, SMN-9	0.15	852	-1.62	1.3	75.4	228	
SMN-2, SMN-4	0.15	804	0.31	1.3	75.2	285	
SMN-3, SMN-5, SMN-6	0.15	806	2.17	1.3	76.2	324	
EBU-1, EBU-8, EBU-9	0.15	858	-1.73	1.9	75.1	160	
EBU-2, EBU-7	0.15	801	-0.09	1.8	75.5	190	
EBU-3, EBU-5, EBU-6	0.15	806	2.16	1.8	75.5	413	
Haplogranite, Binder *et al.* (2018)							
BHG	0.20	850	0.00	1.1	78.4	323	14
BHG	0.20	850	1.95	1.0	78.8	74	5
BNa(d)	0.20	850	0.00	1.0	79.0	84	12
BNa(e)	0.20	850	0.00	1.0	78.8	135	14
BNa(f)	0.20	850	0.00	1.1	78.5	264	25
BNa(g)	0.20	850	1.95	0.9	79.7	128	6
HGP	0.20	850	0.00	0.8	76.9	508	15
HGP	0.20	850	0.00	1.3	80.8	257	17
HGP	0.20	850	1.95	0.8	76.9	246	9
HGP	0.20	850	1.95	1.0	81.8	96	12

Table S-8 continued

Type of glass investigated, reference Run name *(type of partial melt)*	***P*** **GPa**	***T*** **°C**	**log(f_{O2})** **(ΔNNO)**	**Melt alkalinity(a)**	**SiO_2** **mass %(b)**	**$D^{fl/mt}(S_{tot})$**	**1 s.d.(c)**
Trachyte to rhyolite, Masotta *et al.* (2016)							
A18 *(trachy-andesite)*	0.20	950	1.78	0.7	65.1	1.5	0.3
A13 *(trachyte)*	0.20	900	1.86	0.7	63.8	17	3
A15 *(trachyte)*	0.20	850	1.95	0.9	68.2	21	8
D11 *(dacite)*	0.20	900	1.86	0.6	67.9	20	11
D5 *(rhyodacite)*	0.20	850	1.95	0.6	71.7	95	24
RD11 *(rhyolite)*	0.20	900	1.86	0.6	73.2	101	19
RD12 *(rhyolite)*	0.20	800	2.03	0.7	76.6	114	43
***NAS*(h)**, Zajacz (2015)							
248a	0.50	1240	1.33	0.5	73.6	112	
279b	0.50	1240	1.33	0.9	68.8	20	
251b	0.50	1240	1.33	1.1	65.9	4	
250b	0.50	1240	1.33	1.6	60.7	0.9	
250a	0.50	1240	1.33	2.3	56.9	0.3	
255b	0.50	1240	1.33	2.3	58.7	0.3	
Rhyolite, Zajacz *et al.* (2013)							
203 *(rhyolite)*	0.20	1000	-0.8	1.3	76.4	225	13
213 *(rhyolite)*	0.20	1000	-0.8	1.1	77.4	294	24
212 *(rhyolite)*	0.20	1000	-0.8	1.0	77.7	403	25
198 *(rhyolite)*	0.20	1000	-0.8	0.9	77.5	635	80
204 *(rhyolite)*	0.20	1000	-0.8	0.8	76.9	776	148
199 *(rhyolite)*	0.20	1000	-0.8	0.7	69.8	462	73
200 *(andesite)*	0.20	1000	-0.8	0.4	59.9	160	9
201 *(basaltic andesite)*	0.20	1030	-0.8	0.3	55.4	79	4
197 *(rhyolite)*	0.20	900	-0.8	0.9	77.8	652	57
196 *(rhyolite)*	0.20	800	-0.8	0.9	78.2	532	86
Andesite, Zajacz *et al.* (2012)							
145-161, 166, 180, 210-211	0.20	1000	-0.5	0.4	60.7	166	42
163	0.20	1000	-1.2	0.4	60.6	151	18
184	0.20	1000	-0.1	0.3	60.1	97	23
168, 172	0.20	1000	0.3	0.4	60.6	50.5	1.5
162	0.20	1000	0.6	0.3	60.7	30	3
175	0.20	1000	1.8	0.3	60.2	30	2
178	0.20	1000	4.0	0.4	64.4	19	1
Pelite melt, D'Souza and Canil (2018)							
P487a *(rhyolite)*	3.00	1000	>2.7(i)	0.8	73.2	72	12
P498b *(rhyolite)*	3.00	1000	-0.5-2.7(i,j)	0.9	73.2	138	20
P486a *(rhyolite)*	3.00	1050	>2.7(i)	0.9	73.1	69	10
P494b *(rhyolite)*	3.00	950	<-0.5(j)	0.8	73.3	232	40
P490a *(rhyolite)*	3.00	1000	<-0.5(j)	0.8	74.0	159	38
P491a *(rhyolite)*	3.00	1000	<-0.5(j)	0.7	72.7	49	14
P491b *(rhyolite)*	3.00	1000	<-0.5(j)	0.8	73.5	102	11
P497b *(rhyolite)*	3.00	1000	<-0.5(j)	0.8	73.5	111	16
P494a *(rhyolite)*	3.00	950	<-0.5(j)	1.0	73.5	135	22
P495b *(rhyolite)*	3.00	950	<-0.5(j)	0.9	72.9	172	51

Table S-8 continued

Type of glass investigated, reference Run name *(type of partial melt)*	***P*** **GPa**	***T*** **°C**	**log(f_{O2})** **(ΔNNO)**	**Melt alkalinity**(a)	**SiO_2** **mass %**(b)	**$D^{fl/mt}$(S_{tot})**	**1 s.d.**(c)
MORB(k), Jégo and Dasgupta (2013)							
G186 *(rhyolite)*	2.00	800	nb(l), (j)	0.20	77.5	310	170
G187 *(trachy-andesite)*	2.00	1000	nb(l), (j)	0.66	62.2	4179	1069
G195 *(rhyolite)*	2.00	850	-0.69	0.22	78.6	252	128
G190 *(rhyolite)*	2.00	900	-0.47	0.31	76.7	11	351(m)
G207 *(rhyolite)*	2.00	925	-0.52	0.46	75.6	368	203
G193 *(rhyolite)*	2.00	950	-0.71	0.39	75.9	229	288(m)
B93 *(rhyolite)*	2.00	1010	-0.75	0.61	73.4	856	328
B85 *(rhyolite)*	2.00	1050	-0.64	0.56	71.4	646	434
G223 *(rhyolite)*	3.00	950	-1.08	0.35	78.3	810	363
G224 *(rhyolite)*	3.00	1050	-0.73	0.58	75.6	1706	708
G218 *(rhyolite)*	2.00	900	-2.42	0.44	76.8	15	220(m)
G203 *(rhyolite)*	2.00	950	-2.41	0.68	73.1	1205	162
B87 *(rhyolite)*	2.00	1000	-2.72	0.72	73.2	1113	162
G202 *(rhyolite)*	2.00	1050	-2.91	0.81	70.4	1513	336
G225 *(rhyolite)*	3.00	900	-3.05	0.41	77.6	303	153
G228 *(rhyolite)*	3.00	975	-2.86	0.49	76.5	400	150
G230 *(rhyolite)*	3.00	1050	-2.74	0.44	76.7	1189	366
MORB(k), Jégo and Dasgupta (2014)							
G246 *(rhyolite)*	2.00	950	4.3	1.29	70.0	75	32
G246 *(rhyolite)*	2.00	950	4.3	1.29	70.0	75	32
G243 *(trachyte)*	2.00	1050	4.1	0.75	61.9	30	3
G249 *(trachyte)*	3.00	1050	3.5	1.13	66.4	22	5
G251 *(rhyolite)*	3.00	950	3.3	1.22	72.5	51	9
G280 *(trachy-andesite)*	3.00	1050	1.8	0.64	54.4	381	90
G261 *(trachyte)*	3.00	1050	1.25	0.92	61.5	232	99
G277 *(trachy-andesite)*	3.00	1050	-0.8	0.74	57.1	4282	601
G281 *(trachy-andesite)*	3.00	1050	-1.3	0.82	58.1	4636	1837
G264 *(trachyte)*	3.00	1050	-4.8	0.93	62.4	1777	683

(a) Alkalinity = (Na + K) / Al (mol/mol).

(b) Anhydrous basis.

(c) Uncertainty of $D^{fl/mt}$ (where reported in the original studies).

(d) *X*(NaCl) in fluid = 0.3, where *X* is the mole fraction.

(e) *X*(NaCl) in fluid = 0.2.

(f) *X*(NaCl) in fluid = 0.1.

(g) *X*(NaCl) in fluid = 0.1 to 0.3.

(h) Na_2O-Al_2O_3-SiO_2 system.

(i) Anhydrite present.

(j) Pyrrhotite present.

(k) Mid-oceanic ridge basalt.

(l) nb = not buffered: nr = not reported.

(m) These datapoints were omitted from comparisons (Fig. S-5, S-6) because of unphysically large errors yielding negative $D^{fl/mt}$ values.

Supplementary Figures

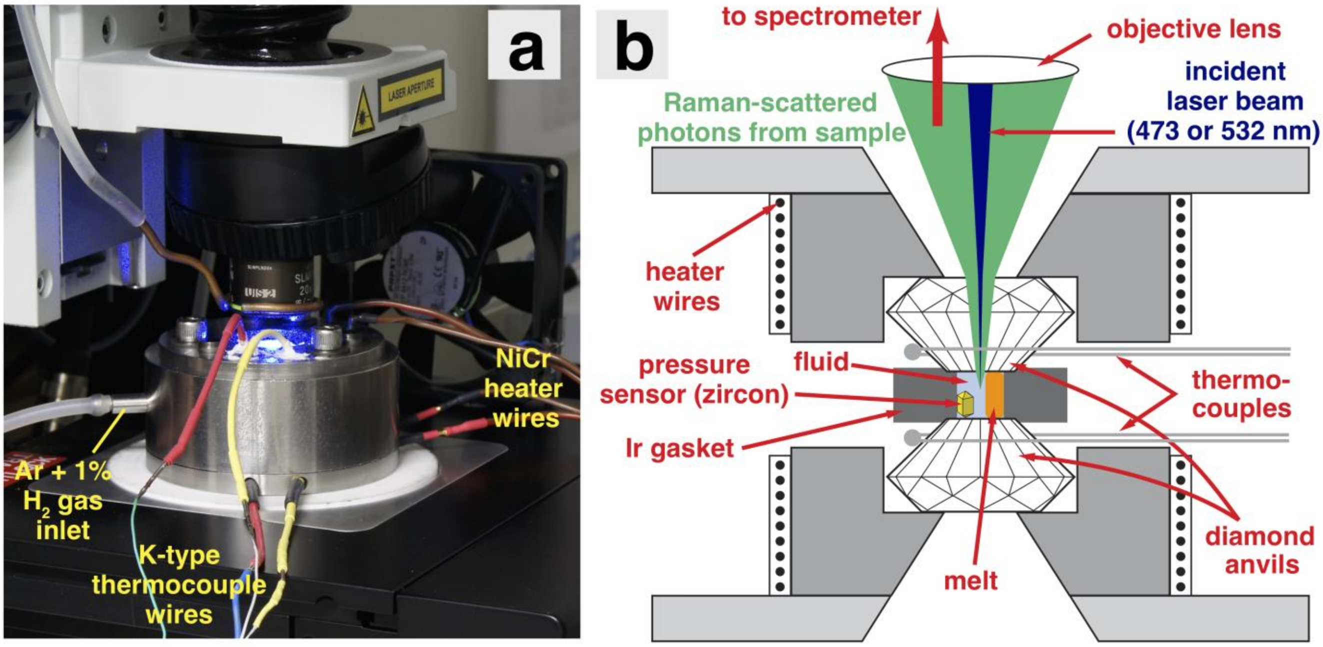

Figure S-1 **(a)** Photograph and **(b)** schematic view of the DAC setup (GFZ, Potsdam) installed at the Raman spectrometer and used in the present study (modified from Schmidt and Chou, 2012).

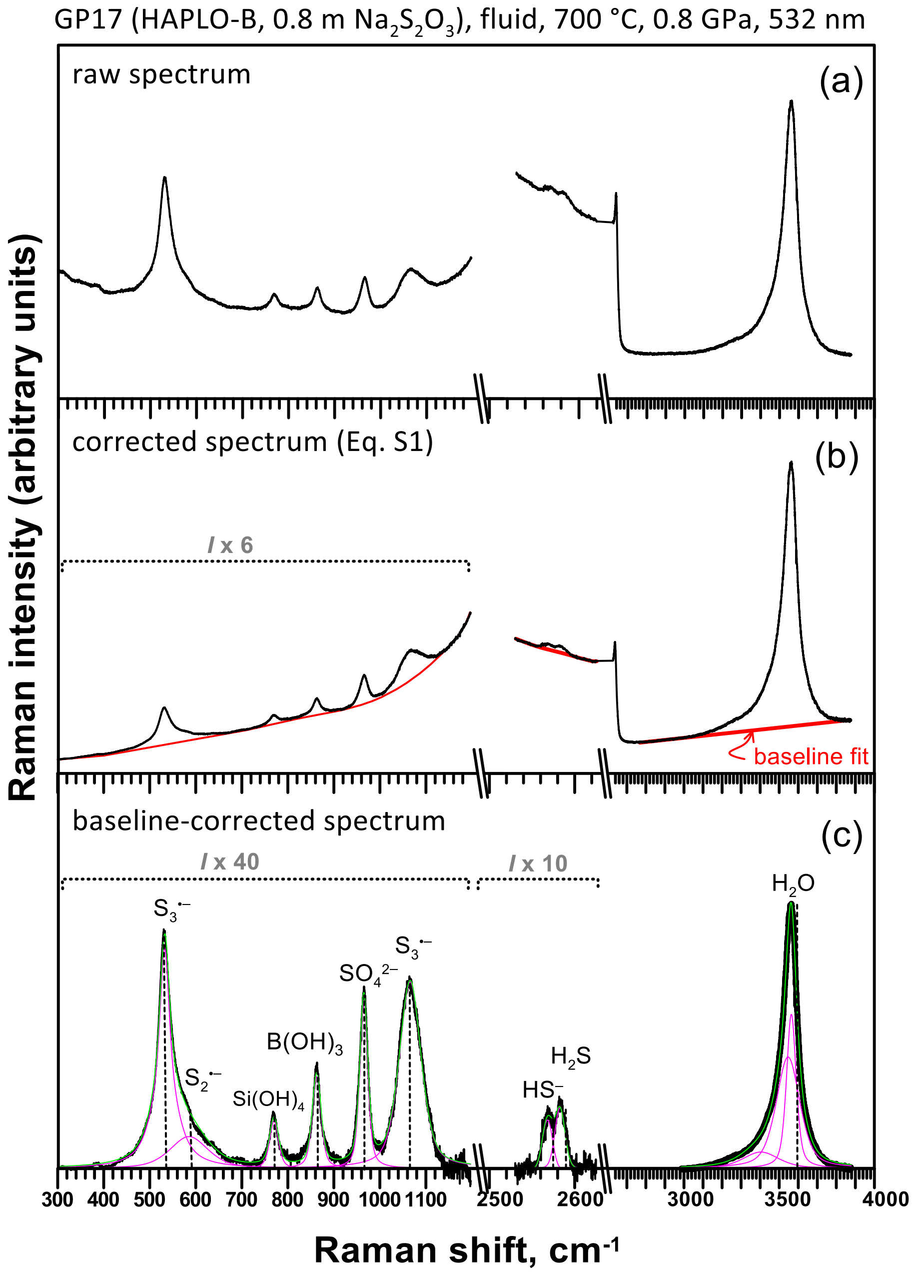

Figure S-2 Illustration of the different steps of Raman spectra processing (correction and fitting), performed in this study. Some spectral regions are scaled by the factor indicated in the figure to better highlight the details.

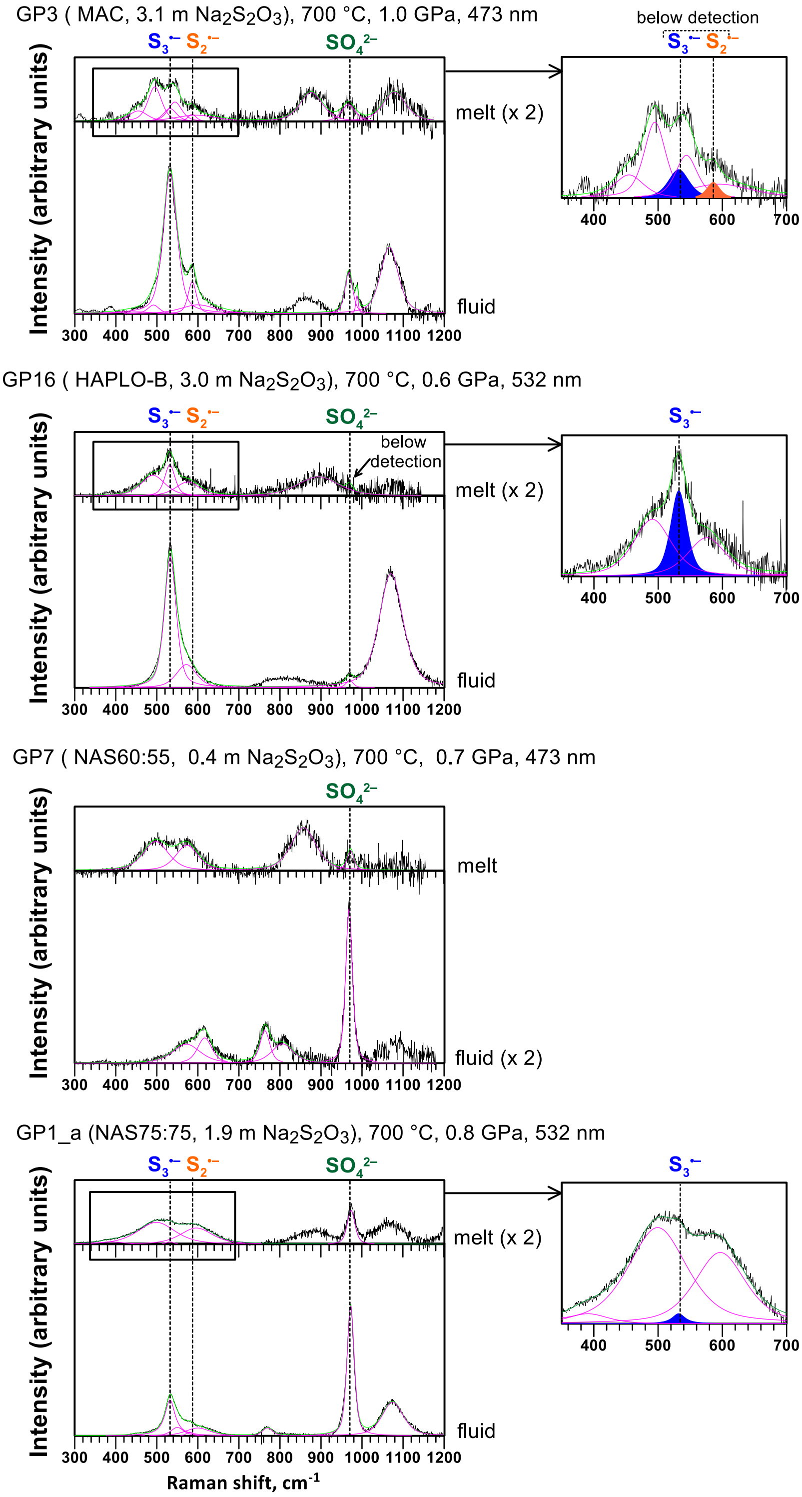

Figure S-3 Example of baseline corrected spectra and their fits in the low wavenumber region (<1200 cm^{-1}) for the coexisting fluid (blue) and melt (red). The zoom in the 350–700 cm^{-1} range of the melt spectra, if the sulfur radicals were detected in the fluid phase, shows least-square fits of the S radical peaks (experiment GP1 and GP16) or, if the S radicals are below detection limit, the peak areas maximum values (experiment GP3). Some spectra are scaled by ×2 to better compare the melt and fluid spectra for each experiment (*e.g.*, experiment GP3, melt ×2).

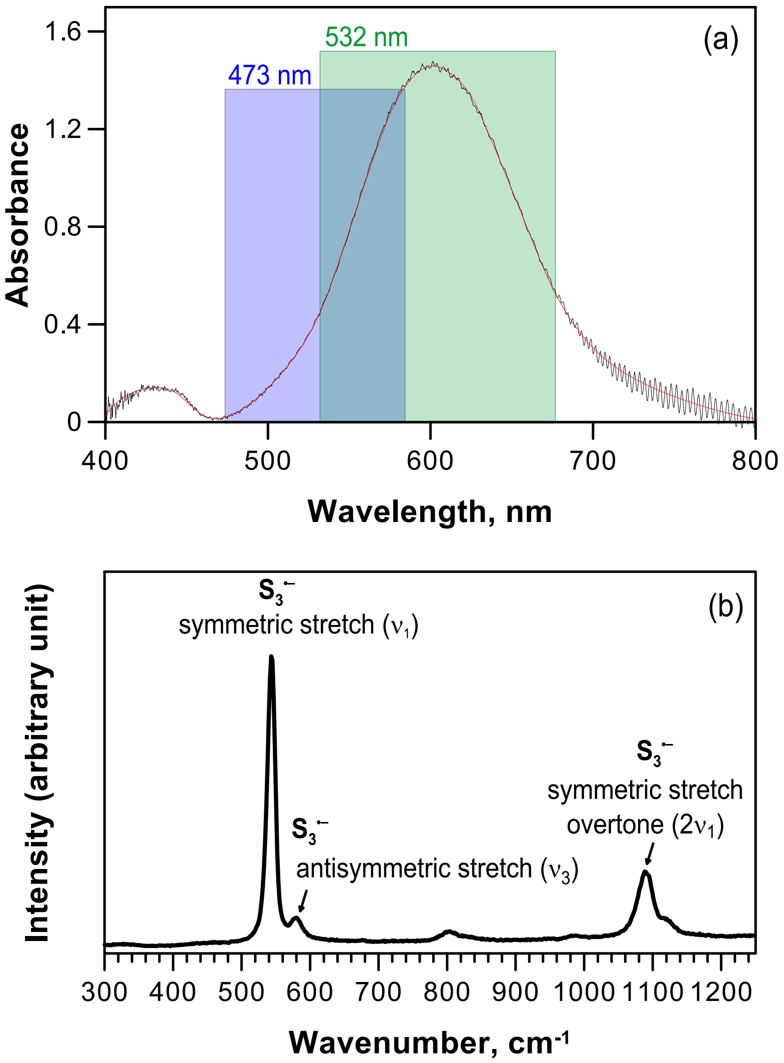

Figure S-4 **(a)** Absorbance spectrum of a 50 µm thick doubly polished section of a lazurite crystal (AMNH) containing $S_3^{\bullet-}$ chromophore, acquired in transmission mode with an Xplora Raman spectrometer. In blue and green are highlighted the wavelength range corresponding to the Raman spectra (0–4000 cm^{-1}) with 473 and 532 nm excitation, respectively. **(b)** Raman spectrum of the same sample (acquisition time 2×10 s, excitation 532 nm).

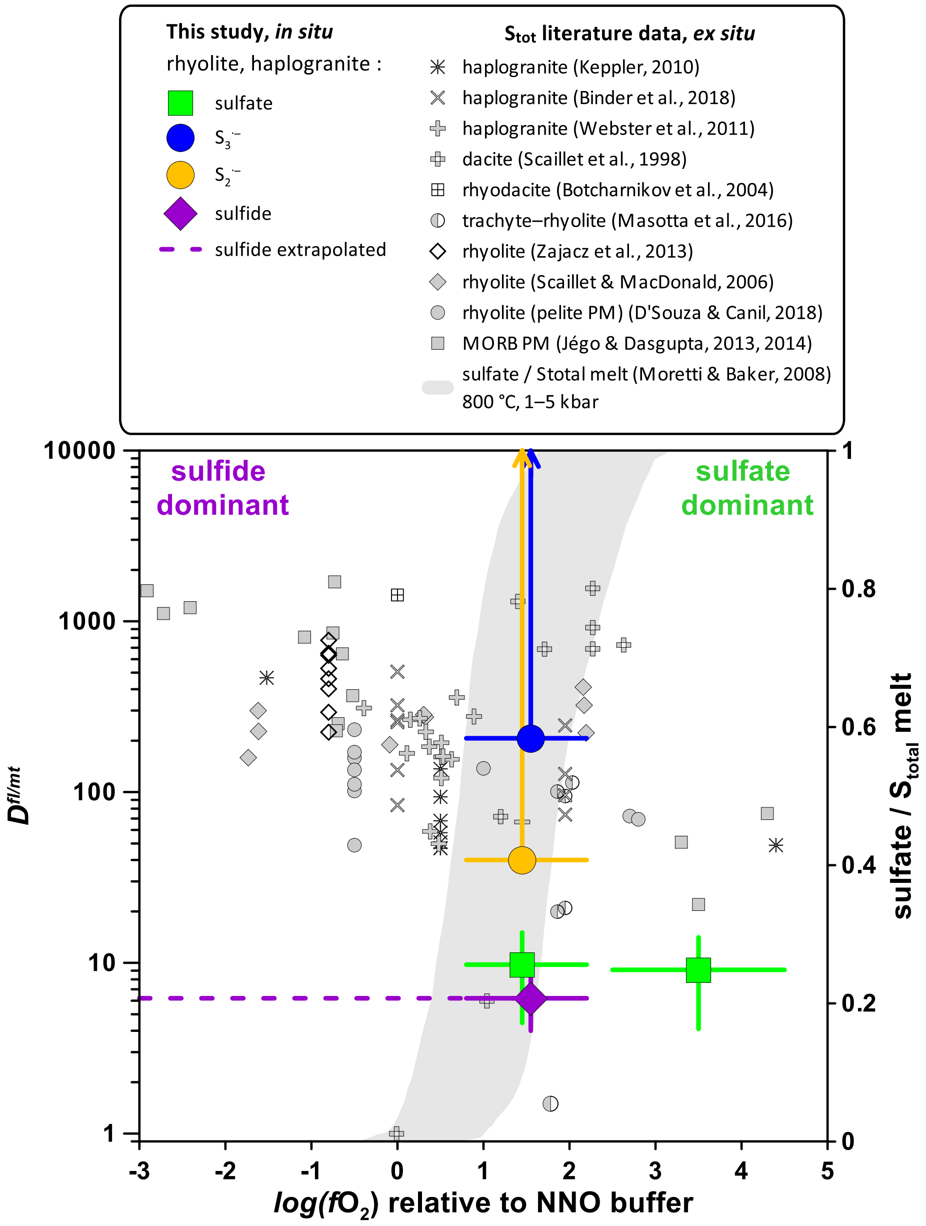

Figure S-5 Comparison of *in situ* fluid/melt partition coefficients of sulfate, sulfide, $S_3^{•-}$ and $S_2^{•-}$, derived in this study for rhyolitic melts (MAC, HAPLO-B) at 700 °C and 0.3–1.5 GPa, with those of total sulfur (S_{tot}) from *ex situ* literature data on moderately alkaline felsic melts typical of natural settings (SiO_2 >65 mass %, alkalinity <1.5) obtained at 0.05–3.0 GPa and 750–1050 °C as a function of f_{O_2}. PM = partial melt. Grey area corresponds to the sulfate-sulfide transition at 800 °C and 0.1–0.5 GPa in water-saturated rhyolite melt according to available theoretical predictions; horizontal dashed line shows partition coefficients for sulfide extrapolated to more reducing conditions than our *in situ* measurements. Error bars are given as 1 s.d.; those of literature data points are omitted for clarity (see Table S-8 for detailed compilation).

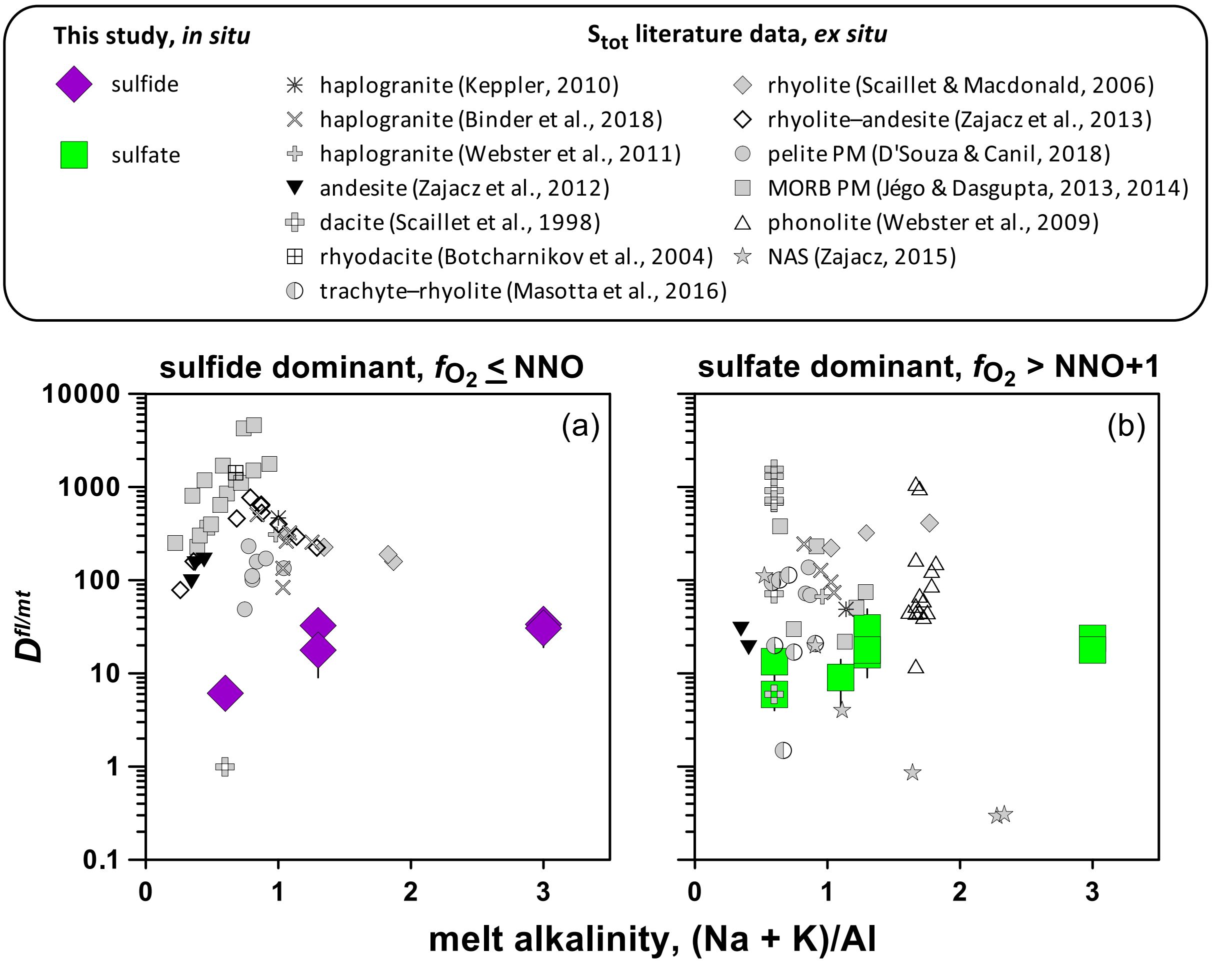

Figure S-6 Comparison of the fluid/melt partition coefficients of **(a)** sulfide and **(b)** sulfate species derived in this study (700°C, 0.3–1.5 GPa) with those reported in the literature (compiled in Table S-8) from quenched experimental products obtained at redox conditions at which either sulfide or sulfate predominate (750–1250°C, 0.05–3.0 GPa), as a function of melt alkalinity, (K + Na) / Al (mol). Error bars for the data from our study are comparable with the symbol size; error bars for the literature data are omitted for clarity. PM = partial melt.

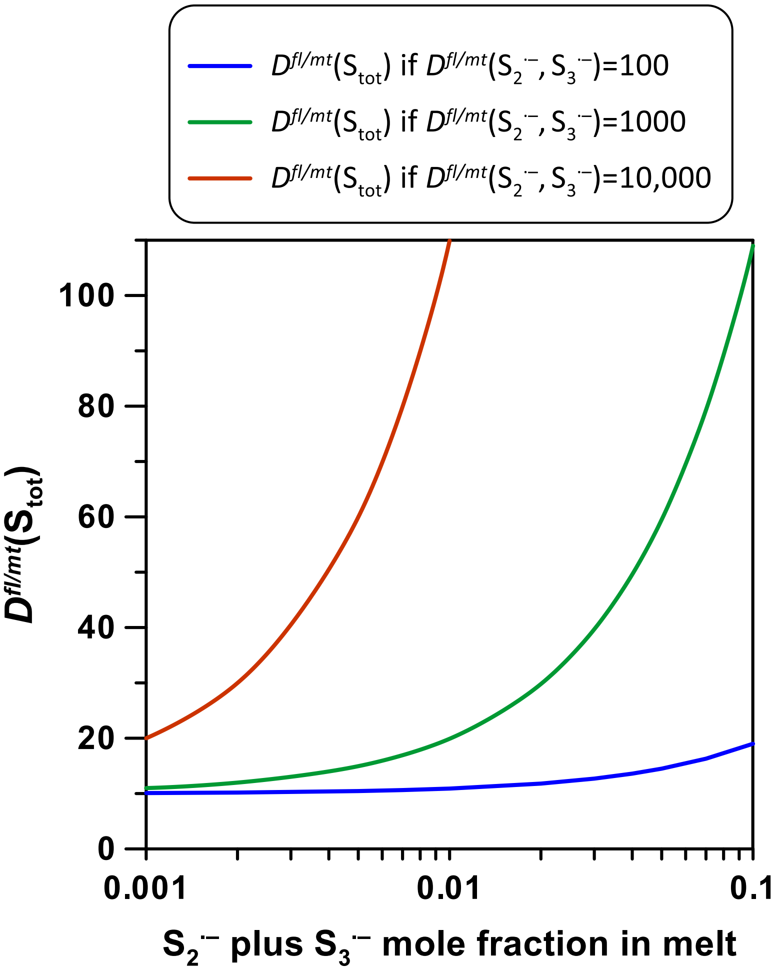

Figure S-7 Estimation of the effect of radical ions on the total sulfur fluid/melt partition coefficient as a function of the ($S_2^{\bullet-}$ + $S_3^{\bullet-}$) mole fraction in melt, and assuming that the mass of the silicate melt reservoir is much bigger than that of the produced aqueous fluid so that the concentrations of S species in the melt remain almost constant when a small amount of fluid is produced, $D^{fl/mt}$(sulfate) = 10; $D^{fl/mt}$(sulfide) = 10, and $D^{fl/mt}$($S_2^{\bullet-}$, $S_3^{\bullet-}$) = 100 (minimal estimate) or 1000 (reasonably possible) or 10,000 (tentative maximal estimate). It can been seen that even small fractions of $S_3^{\bullet-}$ (and $S_2^{\bullet-}$) in melt (<0.01) may increase the overall S partitioning into the fluid by a factor of 2 to 10, compared to $S_3^{\bullet-}$ -free melts. Note that this effect of radical ions is, however, limited to sulfur-rich fluids (> several mass % S_{tot}), in which the radical ions may account for as much as half of total dissolved sulfur (*e.g.*, see Fig. S-8).

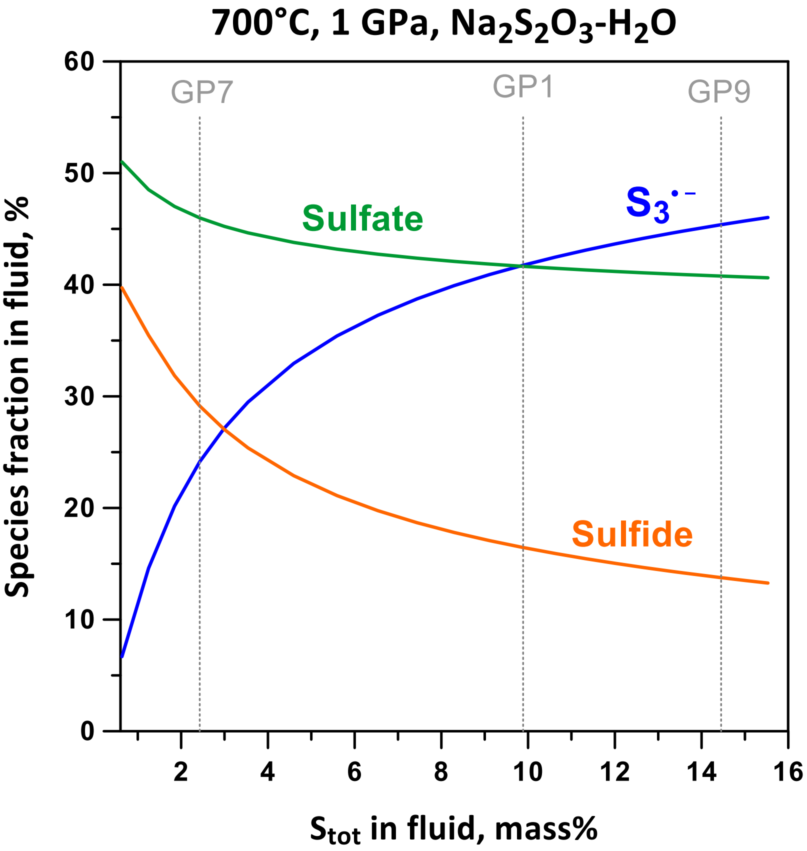

Figure S-8 Abundance of the three major redox forms of sulfur in an aqueous $Na_2S_2O_3$ solution as a function of total sulfur dissolved concentration at 700 °C and 1 GPa, predicted using the thermodynamic properties of $S_3^{\bullet-}$ and other sulfur aqueous species from Pokrovski and Dubessy (2015) that may be extrapolated using the revised and extended HKF model (Sverjensky *et al.*, 2014) to the indicated *T-P* conditions. Vertical dotted lines indicate the total sulfur concentrations of our selected *in situ* experiments across the range covered in this study (see Table S-2). Sulfate (SO_4^{2-}, HSO_4^-, $NaSO_4^-$, and $NaHSO_4$) and sulfide (H_2S, HS^-, and NaHS) stand for the sum of the different (de)protonated species and its alkali ion pairs of the same sulfur redox state. Other redox forms of sulfur (sulfite, polysulfides, and thiosulfate) represent less than 2 % of S_{tot}. For the $S_2^{\bullet-}$ ion, the available thermodynamic data are too limited for predictions to be made at our conditions.

Supplementary Information References

Bassett, W.A., Shen, A.H., Bucknum, M., Chou, I.M. (1993) Hydrothermal studies in a new diamond anvil cell up to 10 GPa and from −190 °C to 1200 °C. In Liebermann, R.C., Sondergeld, C.H. (Eds.) *Experimental Techniques in Mineral and Rock Physics*. Birkhäuser, Basel, 487–495.

Binder, B., Wenzel, T., Keppler, H. (2018) The partitioning of sulfur between multicomponent aqueous fluids and felsic melts. *Contribution to Mineralogy and Petrology* 173, 18.

Borisova, A.Y., Pichavant, M., Beny, J.-M., Rouer, O., Pronost, J. (2005) Constraints on dacite magma degassing and regime of the June 15, 1991, climactic eruption of Mount Pinatubo (Philippines): New data on melt and crystal inclusions in quartz. *Journal of Volcanology and Geothermal Research* 145, 35–67.

Borisova, A.Y., Pokrovski, G.S., Pichavant, M., Freydier, R., Candaudap, F. (2010) Arsenic enrichment in hydrous peraluminous melts: Insights from femtosecond laser ablation-inductively coupled plasma-quadrupole mass spectrometry, and in situ X-ray absorption fine structure spectroscopy. *American Mineralogist* 95, 1095–1104.

Botcharnikov, R.E., Behrens, H., Holtz, F., Koepke, J., Sato, H. (2004) Sulfur and chlorine solubility in Mt. Unzen rhyodacitic melt at 850 C and 200 MPa. *Chemical Geology* 213, 207–225.

Bouhifd, M.A., Whittington, A.G., Richet, P. (2015) Densities and volumes of hydrous silicate melts: New measurements and predictions. *Chemical Geology* 418, 40–50.

Chivers, T., Elder, P.J.W. (2013) Ubiquitous trisulfur radical ion: fundamentals and applications in materials science, electrochemistry, analytical chemistry and geochemistry. *Chemical Society Reviews* 42, 5996–6005.

D'Souza, R.J., Canil, D. (2018) The partitioning of chalcophile elements between sediment melts and fluids at 3 GPa, 950–1050° C with implications for slab fluids in subduction zones. *Earth and Planetary Science Letters* 498, 215–225.

Dargent, M., Dubessy, J., Truche, L., Bazarkina, E.F., Nguyen-Trung, C., Robert, P. (2013) Experimental study of uranyl (VI) chloride complex formation in acidic LiCl aqueous solutions under hydrothermal conditions (T= 21 °C–350 °C, Psat) using Raman spectroscopy. *European Journal of Mineralogy* 25, 765–775.

Driesner, T. (2007) The system H_2O–NaCl. Part II: Correlations for molar volume, enthalpy, and isobaric heat capacity from 0 to 1000 °C, 1 to 5000 bar, and 0 to 1 XNaCl. *Geochimica et Cosmochimica Acta* 71, 4902–4919.

Everall, N.J. (2000) Modeling and measuring the effect of refraction on the depth resolution of confocal Raman microscopy. *Applied Spectroscopy* 54, 773–782.

Haar, L. Gallagher, J.S. Kell, G.S. (1984) NBS/NRC Steam Tables: Thermodynamic and Transport Properties and Computer Programs for Vapor and Liquid States of Water in SI Units. Hemisphere, Washington, DC.

Heinrich, C.A. (1990) The chemistry of hydrothermal tin (-tungsten) ore deposits. *Economic Geology* 85, 457–481.

Holtz, F., Johannes, W., Tamic, N., Behrens, H. (2001) Maximum and minimum water contents of granitic melts generated in the crust: a reevaluation and implications. *Lithos* 56, 1–14.

Iacovino, K., Glass density Calc. v3.2., http://www.kaylaiacovino.com/tools-for-petrologists/ (2017).

Jacquemet, N., Guillaume, D., Zwick, A., Pokrovski, G.S. (2014) In situ Raman spectroscopy identification of the S_3^- ion in S-rich hydrothermal fluids from synthetic fluid inclusions. *American Mineralogist* 99, 1109–1118.

Jégo, S., Dasgupta, R. (2013) Fluid-present melting of sulfide-bearing ocean-crust: Experimental constraints on the transport of sulfur from subducting slab to mantle wedge. *Geochimica et Cosmochimica Acta* 110, 106-134.

Jégo, S., Dasgupta, R. (2014) The fate of sulfur during fluid-present melting of subducting basaltic crust at variable oxygen fugacity. *Journal of Petrology* 55, 1019–1050.

Keppler, H. (2010) The distribution of sulfur between haplogranitic melts and aqueous fluids. *Geochimica et Cosmochimica Acta* 74, 645–660.

Knoche, R., Webb, S.L., Dingwell, D.B. (1992) A partial molar volume for B_2O_3 in haplogranitic melt. *Canadian Mineralogist* 3, 561–569.

Kokh, M.A., Assayag, N., Mounic, S., Cartigny, P., Gurenko, A., Pokrovski, G.S. (2020) Multiple sulfur isotope fractionation in hydrothermal systems in the presence of radical ions and molecular sulfur. *Geochimica et Cosmochimica Acta* (in press), doi: 10.1016/j.gca.2020.06.016.

Lange, R.L., Carmichael, I.S. (1990) Thermodynamic properties of silicate liquids with emphasis on density, thermal expansion and compressibility. *Reviews in Mineralogy and Geochemistry* 24, 25–64.

Le Losq, C., Neuville, D.R., Florian, P., Henderson, G.S., Massiot, D. (2014) The role of Al3+ on rheology and structural changes in sodium silicate and aluminosilicate glasses and melts. *Geochimica et Cosmochimica Acta* 126, 495–517.

Ledé, B., Demortier, A., Gobeltz-Hautecoeur, N., Lelieur, J.-P., Picquenard, E., Duhayon, C. (2007) Observation of the ν_3 Raman band of S_3^- inserted into sodalite cages. *Journal of Raman Spectrosopy* 38, 1461–1468.

Linke, W.F., Seidell, A. (1965) Solubilities of Inorganic and Metal-Organic Compounds: a Compilation of Solubility Data from the Periodical Literature. 4th edition, American Chemical Society, Washington.

Malfait, W.J., Seifert, R., Petitgirard, S., Perrillat, J.-P., Mezouar, M., Ota, T., Nakamura, E., Lerch, P., Sanchez-Valle, C. (2014) Supervolcano eruptions driven by melt buoyancy in large silicic magma chambers. *Nature Geoscience* 7, 122.

Masotta, M., Keppler, H., Chaudhari, A. (2016) Fluid-melt partitioning of sulfur in differentiated arc magmas and the sulfur yield of explosive volcanic eruptions. *Geochimica et Cosmochimica Acta* 176, 26–43.

Moretti, R., Baker, D.R. (2008) Modeling the interplay of fO_2 and fS_2 along the FeS-silicate melt equilibrium. *Chemical Geology* 256, 286–298.

Mysen, B.O. (2007) The solution behavior of H_2O in peralkaline aluminosilicate melts at high pressure with implications for properties of hydrous melts. *Geochimica et Cosmochimica Acta* 71, 1820–1834.

Mysen, B.O., Wheeler, K. (2000) Solubility behavior of water in haploandesitic melts at high pressure and high temperature. *American Mineralogist* 85, 1128–1142.

Ochs, F.A., Lange, R.A. (1999) The density of hydrous magmatic liquids. *Science* 283, 1314–1317.

Pichavant, M. (1987) Effects of B and H_2O on liquidus phase relations in the haplogranite system at l kbar. *American Mineralogist* 72, 1056–1070.

Picon, M. (1924) Sur les Hydrates de l'Hyposulfite de Sodium. Masson, Paris.

Pokrovski, G.S., Tagirov, B.R., Schott, J., Hazemann, J.-L., Proux, O. (2009) A new view on gold speciation in sulfur-bearing hydrothermal fluids from in-situ X-ray absorption spectroscopy and quantum-chemical modeling. *Geochimica et Cosmochimica Acta* 73, 5406–5427.

Pokrovski, G.S., Dubessy, J. (2015) Stability and abundance of the trisulfur radical ion in hydrothermal fluids. *Earth and Planetary Science Letters* 411, 298–309.

Scaillet, B., Clémente, B., Evans, B.W., Pichavant, M. (1998) Redox control of sulfur degassing in silicic magmas. *Journal of Geophysical Research* 103, 23937–23949.

Scaillet, B., Macdonald, R. (2006) Experimental and thermodynamic constraints on the sulphur yield of peralkaline and metaluminous silicic flood eruptions. *Journal of Petrology* 47, 1413–1437.

Schmidt, C. (2009) Raman spectroscopic study of a H_2O + Na_2SO_4 solution at 21–600 °C and 0.1 MPa to 1.1 GPa. Relative differential ν_1-SO_4^{2-} Raman scattering cross sections and evidence of the liquid-liquid transition. *Geochimica et Cosmochimica Acta* 73, 425–437.

Schmidt, C., Chou, I.-M. (2012) The Hydrothermal Diamond Anvil Cell (HDAC) for Raman spectroscopic studies of geological fluids at high pressures and temperatures. In Dubessy, J., Caumon, M.-C., Rull, F. (Eds.) *Raman Spectroscopy Applied to Earth Sciences and Cultural Heritage*. Mineralogical Society of Great Britain and Ireland, vol. 12, 247–276.

Schmidt, C., Steele-MacInnis, M., Watenphul, A., Wilke, M. (2013) Calibration of zircon as a Raman spectroscopic pressure sensor to high temperatures and application to water-silicate melt systems. *American Mineralogist* 98, 643–650.

Schmidt, C., Seward, T.M. (2017) Raman spectroscopic quantification of sulfur species in aqueous fluids: Ratios of relative molar scattering factors of Raman bands of H_2S, HS^-, SO_2, HSO_4^-, SO_4^{2-}, $S_2O_3^{2-}$, S_3^- and H_2O at ambient conditions and information on changes with pressure and temperature. *Chemical Geology* 467, 64–75.

Seel, F. (1984) Sulfur in artwork: Lapis Lazuli and ultramarine pigments. *Studies in Inorganic Chemistry* 5, 67–89.

Shvarov, Y.V. (2008) HCh: new potentialities for the thermodynamic simulation of geochemical systems offered by Windows. *Geochemistry International* 46, 834-839.

Shvarov, Y.V. (2015) A suite of programs, OptimA, OptimB, OptimC, and OptimS, compatible with the Unitherm database, for deriving the thermodynamic properties of aqueous species from solubility, potentiometry and spectroscopy measurements. *Applied Geochemistry* 55, 17-27.

Steele-MacInnis, M., Schmidt, C. (2014) Silicate speciation in H_2O-Na_2O-SiO_2 fluids from 3 to 40 mol % SiO_2, to 600 °C and 2 GPa. *Geochimica et Cosmochimica Acta* 136, 126–141.

Sverjensky, D.A., Harrison, B., Azzolini, D. (2014) Water in the deep Earth: The dielectric constant and the solubilities of quartz and corundum to 60 kb and 1200 °C. *Geochimica et Cosmochimica Acta* 129, 125-145.

Toplis, M.J., Dingwell, D.B., Hess, K.U., Lenci, T. (1997) Viscosity, fragility, and configurational entropy of melts along the join SiO_2-$NaAlSiO_4$. *American Mineralogist* 82, 979–990.

Webster, J.D., Sintoni, M.F., De Vivo, B. (2009) The partitioning behavior of Cl, S, and H_2O in aqueous vapor-±saline-liquid saturated phonolitic and trachytic melts at 200 MPa. *Chemical Geology* 263, 19–36.

Webster, J.D., Goldoff, B., Shimizu, N. (2011) C-O-H-S fluids and granitic magma: how S partitions and modifies CO_2 concentrations of fluid-saturated felsic melt at 200 MPa. *Contribution to Mineralogy and Petrology* 162, 849–865.

Wojdyr, M. (2010) Fityk: a general-purpose peak fitting program. *Journal of Applied Crystallography* 43, 1126–1128.

Zajacz, Z., Candela, P.A., Piccoli, P.M., Sanchez-Valle, C. (2012) The partitioning of sulfur and chlorine between andesite melts and magmatic volatiles and the exchange coefficients of major cations. *Geochimica et Cosmochimica Acta 89*, 81–101.

Zajacz, Z., Candela, P. A., Piccoli, P. M., Sanchez-Valle, C., Wälle, M. (2013) Solubility and partitioning behavior of Au, Cu, Ag and reduced S in magmas. *Geochimica et Cosmochimica Acta* 112, 288–304.

Zajacz, Z. (2015) The effect of melt composition on the partitioning of oxidized sulfur between silicate melts and magmatic volatiles. *Geochimica et Cosmochimica Acta* 158, 223–244.